JGR Atmospheres

RESEARCH ARTICLE
10.1029/2025JD043961

**Special Collection:**
Recent progress in atmospheric boundary layer turbulence and implications to surface-atmosphere exchange

# Quantifying High-Frequency Turbulence Energy in the Atmosphere and Its Impact on Near-Surface Diffusion: Parameterization Scheme and Validation in WRF-Chem

**Liu Zhenxin[1], Zhang Wenxi[1], Liu Lei[2], Li Xiaolan[1,3], Mao Yuhao[1], and Liao Hong[1]**

[1]Jiangsu Key Laboratory of Atmospheric Environment Monitoring and Pollution Control/Jiangsu Collaborative Innovation Center of Atmospheric Environment and Equipment Technology, School of Environmental Science and Engineering, Nanjing University of Information Science and Technology (NUIST), Nanjing, China, [2]Laboratory of Atmospheric Physics and Chemistry (LAPC), Institute of Atmospheric Physics, Chinese Academy of Sciences, Beijing, China, [3]Institute of Atmospheric Environment, China Meteorological Administration, Shenyang, China

**Key Points:**

- Wind speed sampling frequency affects small-scale eddy detection, missing 10%–37% turbulent kinetic energy (TKE)
- Based on turbulence energy spectrum theory, missed high-frequency TKE is supplemented, and the new scheme is coupled into WRF-Chem
- This improves TKE and turbulence diffusion coefficient ($K_m$), reducing pollutant concentration bias from 23.77% to 6.18%

**Supporting Information:**

Supporting Information may be found in the online version of this article.

**Correspondence to:**

L. Zhenxin,
liuzhenxin@nuist.edu.cn

**Citation:**

Zhenxin, L., Wenxi, Z., Lei, L., Xiaolan, L., Yuhao, M., & Hong, L. (2025). Quantifying high-frequency turbulence energy in the atmosphere and its impact on near-surface diffusion: Parameterization scheme and validation in WRF-chem. *Journal of Geophysical Research: Atmospheres*, *130*, e2025JD043961. https://doi.org/10.1029/2025JD043961

Received 26 MAR 2025
Accepted 9 SEP 2025

**Author Contributions:**

**Conceptualization:** Liu Zhenxin
**Data curation:** Zhang Wenxi, Liu Lei, Li Xiaolan
**Formal analysis:** Liu Zhenxin, Zhang Wenxi
**Funding acquisition:** Liao Hong
**Investigation:** Zhang Wenxi
**Methodology:** Liu Zhenxin, Liu Lei
**Resources:** Liu Lei, Li Xiaolan
**Supervision:** Liao Hong
**Validation:** Zhang Wenxi, Mao Yuhao
**Visualization:** Zhang Wenxi
**Writing – original draft:** Zhang Wenxi



**Abstract** Atmospheric turbulence is a key meteorological factor influencing the diffusion of urban near-surface air pollution. The turbulence energy spectrum characterizes the distribution of turbulent kinetic energy (TKE) across different eddy scales, with the total energy affecting the diffusion coefficient and pollutant dispersion. Current methods for calculating TKE are sensitive to the temporal resolution of wind speed data, and the limited sampling frequency of instruments is much lower than the dissipation scale. Thus, the high-frequency turbulence energy is missed, and the total TKE is underestimated. To address this issue, this study used high (~10 Hz) and low (~0.05 Hz) frequency wind observations from the Beijing 325-m meteorological tower to assess how sampling frequencies impact TKE calculations. The −5/3 law of the turbulence spectrum was applied to estimate the relationship between observed and theoretical total TKE, and a parameterization scheme was completed. Results showed that the underestimation due to sampling frequency limitations ranges from 10% to 37%, with higher proportions during night and winter. Then a correction factor (HTMC) was incorporated into the BouLac PBL scheme in WRF-Chem. Sensitivity simulations of a heavy haze event in Shenyang were set. The experimental group (EXP) showed lower concentrations of $PM_{2.5}$ near the surface and higher in higher altitudes than those in control group (CTR) during night, indicating stronger vertical turbulent transport. The concentrations in EXP better match observations, with simulation bias reduced from 23.77% to 6.18%. This work provides new insights into urban turbulence transport mechanisms and benefits to improvements in air quality forecasting.

**Plain Language Summary** Atmospheric turbulence influences the diffusion of urban near-surface air pollution in cities and surrounding areas. However, current methods for calculating atmospheric turbulent kinetic energy (TKE) miss the high-frequency turbulence, leading to the underestimation of high-frequency TKE, which in turn affects atmospheric pollution forecasts. Using high- and low-frequency wind data from a Beijing meteorological tower, it is found that the limited sampling frequency leads to missing 10%–37% of TKE, especially during night and winter. To improve prediction accuracy, a correction factor was added to the BouLac scheme in WRF-Chem, which significantly improved the simulated TKE and $K_m$. The bias of simulated $PM_{2.5}$ concentration reduced from 23.77% to 6.18%. This research helps understanding how turbulence affects air pollution near the surface and provides insights for better air quality forecasting.

## 1. Introduction

Atmospheric turbulence is a crucial physical mechanism influencing the dispersion and transport of urban low-level air pollutants (Huszar et al., 2020; Li et al., 2023; Wei et al., 2018; Zhong et al., 2018). Turbulent Kinetic Energy (TKE) directly affects the atmospheric turbulence diffusion capacity, playing a significant role in the migration, diffusion, and spatiotemporal distribution of pollutants (Li et al., 2021; Liu et al., 2018; Ren, Zhang, Wei, Wu, Cai, et al., 2019). Studies have shown that TKE and the turbulence diffusion coefficient ($K_m$) exhibit similar vertical distributions during both day and night. As TKE increases, $K_m$ also increases, meaning that the atmospheric diffusion capacity strengthens with the increase in TKE (Kim et al., 2023). During the development and accumulation of heavy pollution events, turbulence energy is typically low, leading to a lower atmospheric boundary layer height, poorer diffusion capacity, and the accumulation of pollutants near the surface. As TKE and atmospheric diffusion capacity gradually increase, pollutant concentrations decrease until the pollution event

**Writing – review & editing:** Liu Zhenxin, Zhang Wenxi, Mao Yuhao

subsides (Q. Li et al., 2020; Ren, Zhang, Wei, Wu, Liu, et al., 2019; Zhao et al., 2020). Therefore, accurately calculating TKE and $K_m$ is essential for simulating the spatiotemporal distribution of near-surface air pollutant concentrations in air quality modeling.

Atmospheric turbulence exhibits self-organization, meaning that large-scale turbulent eddies naturally break down into smaller-scale vortices, with energy being transferred from larger to smaller scales in a process known as the energy cascade (Dong et al., 2020; Josserand et al., 2017; Vassilicos, 2015). However, under the influence of thermal gradients, an inverse cascade process may also occur, in which small-scale turbulent eddies transfer energy to larger scales (Obukhov, 1971; Zilitinkevich et al., 2013). In the above process, the smallest scale of turbulence, known as the dissipation scale, is determined by both atmospheric viscosity and the turbulence dissipation rate. Below this scale, turbulent energy is dissipated by air viscosity and converted into internal energy (Bodini et al., 2019; Mccaffrey et al., 2017). The spatiotemporal distribution of urban TKE is influenced by the urban low-level thermodynamic and dynamic mechanisms, exhibiting significant spatial and temporal heterogeneity (Y. Liu et al., 2023; Lv et al., 2021). In urban canyons, the complex distribution of buildings and other surface features increases surface roughness, resulting in more intense atmospheric shear and promoting the generation of mechanical turbulence (Li & Katul, 2022). Aliabadi et al. (2021) further quantified the budget of turbulence kinetic energy and heat in the urban roughness sublayer, confirming that shear-induced turbulence generated by mechanical processes within street canyons, as well as its vertical transport within the boundary layer, plays a critical role in turbulence and heat exchange. At the same time, the intense anthropogenic heat release in urban areas creates a more complex and heterogeneous thermal distribution compared to natural surfaces, enhancing atmospheric buoyancy and promoting the generation of thermal turbulence (Heinl et al., 2015; Xu et al., 2024). These factors together lead to a more active generation and energy cascade process of near-surface urban atmospheric turbulence, with greater instability and higher TKE, compared to natural surfaces (Krayenhoff et al., 2015; Monnier et al., 2018).

The turbulence parameterization schemes widely used in current mesoscale atmospheric models are typically based on the first-order closure model (e.g., K-theory) (Holtslag & Boville, 1993; Pielke & Mahrer, 1975), the 1.5-order closure model (e.g., K-l and K-ε models) (Chiravalle, 2006; Martilli et al., 2002; Wu et al., 2024), or higher-order closure model (Nakanishi & Niino, 2009; Shi et al., 2021; Wu et al., 2024). These schemes parameterize turbulent fluctuations, turbulence structure, and turbulent energy by using mean meteorological variables such as wind speed and temperature. On one hand, these schemes are more suitable for horizontally homogeneous surfaces and stable or neutral atmospheric stratification due to the assumptions of the mathematical and physical models (Ma et al., 2024; Zhang et al., 2024). In particular, the direct application of these methods to urban street canyons, which are influenced by complex, heterogeneous building and canyon canopy structures that lead to a more dynamic turbulence energy cascade process, may not be entirely appropriate (Barlow, 2014; Yao et al., 2024). On the other hand, studies have shown that TKE derived from different sampling frequencies exhibits significant differences in both intensity and energy spectrum distribution (Acosta et al., 2024; Xian, Luo, et al., 2024). It is particularly significant in deriving urban near-surface TKE, where it is characterized by spatial heterogeneity in surface geometric structure and thermodynamic properties (Kit et al., 2017; Theuerkauf et al., 2011). This difference is likely attributable to the inadequate consideration of small-scale turbulent eddies during observational sampling, resulting in an underestimation of high-frequency TKE contributions to the total energy spectrum. However, previous turbulence parameterization schemes have not sufficiently considered this mechanism, leading to underestimation in the simulation of TKE and $K_m$ (Honnert, 2019; Honnert et al., 2021; Xian, Luo, et al., 2024), which in turn affects the accuracy of simulating the near-surface atmospheric pollutant dispersion at nighttime (Du et al., 2020; Wang et al., 2021). Recent studies have tried to improve the underestimation of TKE and $K_m$ by adjusting the description of turbulence length scales (Huang & Peng, 2017; Shao et al., 2024), modifying the minimum value of the $K_m$ (Du et al., 2020; Wang et al., 2021), and increasing model resolution (Xu et al., 2021). Despite this, significant improvements are still needed (Du et al., 2020; Jia et al., 2021; Wang et al., 2021).

To address the above-mentioned issues, this study first utilized high-frequency (10 Hz, by ultrasonic anemometer) and low-frequency (0.05 Hz, by cup anemometer) wind speed data sampled at 47, 80, and 140 m heights of the Beijing 325 m meteorological tower. The observed TKE of two different cutoff frequencies was calculated, and the differences between these data at various heights and temporal scales were analyzed. Furthermore, the theoretical full-spectrum TKE was estimated by using the −5/3 law of the turbulence energy spectrum, and the quantitative relationship between TKE derived from different sampling frequencies and the theoretical full-

spectrum TKE was compared, with a focus on its diurnal hourly variations and seasonal changes. Based on this quantitative relationship, a parameterization scheme was introduced into the Bougeault-Lacarrere (BouLac) PBL scheme of the WRF-Chem model, thereby improving the ability of the scheme to simulate the TKE and $K_m$. Finally, the effects and mechanisms of high-frequency turbulent kinetic energy on near-surface turbulence diffusion strength, vertical transport of atmospheric pollutants, and concentration distribution in urban areas were verified by comparing the simulation results of the experimental and control groups in the WRF-Chem model, as well as by comparing them with observed data of near-surface urban air pollutant concentrations.

## 2. Data, Methods, and Model

### 2.1. Description of Observational Data

The wind speed data used in this study for the assessment of high-frequency turbulent kinetic energy as a percentage of total TKE was obtained from the 325-m meteorological tower of the Institute of Atmospheric Physics, Chinese Academy of Sciences (39.96°N, 116.36°E). The heights of the buildings surrounding the tower range from 10 to 80 m, with the tallest building located about 100 m to the south of the tower. The tower is equipped with 15 observation platforms, located at heights of 8, 15, 32, 47, 65, 80, 100, 120, 140, 160, 180, 200, 240, 280, and 320 m. Each platform is equipped with cup anemometers (010C, Metone, USA) with the sampling frequency of 0.05 Hz and the wind speed resolution of 0.1 m $s^{-1}$. Additionally, three-dimensional ultrasonic anemometers (Windmaster Pro, Gill, UK) with the sampling frequency of 10 Hz and the wind speed resolution of 0.1 m $s^{-1}$ were installed on the 47-m, 80-m, and 140-m platforms (Chen et al., 2018; L. Liu et al., 2023; Shi et al., 2019). The high-frequency and low-frequency turbulence data used in this study were collected from the ultrasonic anemometers and cup anemometers at the aforementioned heights, respectively. The analysis periods cover 30 January 2015, to 2 March 2015 (Julian days 30–62) and 4 July 2018, to 12 August 2018 (Julian days 186–225), representing winter period (W period) and summer period (S period) climatic conditions, respectively, to investigate the diurnal and seasonal variations of high-frequency and low-frequency turbulence energy.

In this study, hourly observations of the meteorological variables, such as near-surface wind speed, near-surface temperature and atmospheric boundary layer height, and the air pollutant concentration, such as $PM_{2.5}$ and $NO_2$ concentrations, were applied in the numerical cases for the validation of the improvement of the turbulence scheme. Among them, the near-surface $PM_{2.5}$ and $NO_2$ concentrations in Shenyang were obtained from the Liaoning real-time air quality publishing system (http://211.137.19.74:8089/). The Thermo Fisher Scientific (USA) instruments: 5030i-DHVAA $PM_{2.5}$ Analyzer and 5014i Beta Attenuation Particulate Monitors were used to measure the concentrations at 11 monitoring stations in Shenyang, and then the average of hourly data from different stations was used in this study. The instruments continuously recorded hourly-resolved mass concentrations of $PM_{2.5}$ (μg $m^{-3}$), with data streams transmitted to a central server via Ethernet-based remote telemetry. To ensure measurement integrity, we implemented a rigorous quality assurance protocol: Monthly calibrations using NIST-traceable reference filters were conducted, while real-time environmental interference was mitigated through integrated correction systems (Dynamic Heating System for the 5030i-DHVAA and Humidity Control Module for the 5014i). For the limited communication interruptions observed (<3% of total data), values were reconstructed using linear interpolation from adjacent stations. The hourly mean wind speed (WS) and near-surface temperature (T) were from the national weather stations. A more detailed description of the observational setup and site information can be found in Li et al. (2017).

Meanwhile, the vertical profiles of $PM_{2.5}$ concentrations were measured by a laser particle matter sensor (Plantower PMS-5003T, China), with the detection resolution and range of 1 μg $m^{-3}$ and 0–500 μg $m^{-3}$, respectively. The sensor was attached to an observation balloon. The balloon was released from the balloon-sounding station (41.68°N, 123.42°E) in Shenyang at 02:00, 08:00, 14:00, and 20:00 local time (LT). Detailed information on the laser particle matter sensor and the balloon sounding station can be found in Li et al. (2019).

In this study, the observed atmospheric boundary layer height (ABLH) is estimated using the bulk Richardson number (Ri) approach, as proposed by Vogelezang and Holtslag (1996), which utilizes the vertical profiles of potential temperature and wind speed from observations.

$$\mathrm{Ri}(z) = \frac{\left(\frac{g}{\theta_{vs}}\right)(\theta_{vz} - \theta_{vs})(z - z_s)}{(u_z - u_s)^2 + (v_z - v_s)^2 + bu_*{}^2} \quad (1)$$

Here, $z$ and $s$ denote the height above the ground and the surface, respectively. $g$ refers to the gravitational acceleration, $\theta_v$ is the virtual potential temperature, $u$ and $v$ represent the components of wind speed, $u_*$ is the friction velocity near the surface, and $b$ is a constant. Since $bu_*$ is significantly smaller compared to the wind shear term, it can be reasonably neglected. In this approach, the ABLH is defined as the lowest level at which the Ri reaches a critical threshold. Based on previous studies (Guo et al., 2016; Huo et al., 2021), this critical value is set to 0.25 in this study.

The simulation cases in this study employed the BouLac PBL scheme, which is a local closure scheme of 1.5th order. In this scheme, the ABLH is diagnosed using a threshold of turbulent kinetic energy; specifically, ABLH is identified as the altitude where TKE decreases below 0.005 $m^2\ s^{-2}$ (Banks et al., 2016).

All observational data used in this study have been uploaded to Zenodo, as detailed in the Data/Codes Availability section.

### 2.2. Quality Control Methods for Observational Data

The reliability of wind speed time series largely determines the accuracy of turbulence parameterization. In this study, quality control was applied to both high-frequency and low-frequency wind speed data. First, missing data were filled using multiple imputation based on the Monte Carlo technique (Junninen et al., 2004). Second, the standard deviation of 30-min intervals was calculated, and observations deviating by more than three standard deviations from the mean were removed (Xian, Lu, et al., 2024; Xian, Luo, et al., 2024) and subsequently filled using the aforementioned method.

### 2.3. Turbulence Scale Spectral Analysis Method Based on Wind Speed Time Series

The total turbulent kinetic energy ($\mathrm{TKE}_t$) in the atmosphere can be calculated based on the turbulent power spectrum as follows:

$$\mathrm{TKE}_t = B\int_{k_s}^{k_\epsilon} E(k)\,d(k) \quad (2a)$$

where $\mathrm{TKE}_t$ represents the total turbulent kinetic energy in the atmosphere, and $E(k)$ is the turbulent energy spectrum, which describes the energy distribution of turbulence across different wavenumbers (Ruan et al., 2014). Here, $k_s$ corresponds to the wavenumber of the largest turbulent eddies, and its scale is approximately equal to the street width within the urban canopy. $k_\epsilon$ denotes the wavenumber corresponding to the dissipation frequency of the turbulent energy spectrum in the atmosphere. The coefficient $B$ is calculated as detailed in Text S1 in Supporting Information S1.

The turbulent kinetic energy derived from observational instruments ($\mathrm{TKE}_{\mathrm{obs},\lambda}$) is given by:

$$\mathrm{TKE}_{\mathrm{obs},\lambda} = B\int_{k_s}^{k_\lambda} E(k)\,d(k) \quad (2b)$$

where $\lambda$ represents the sampling cutoff frequency of the observational instruments, and the other symbols are consistent with Equation 2a.

Therefore, on one hand, $\mathrm{TKE}_{\mathrm{obs},\lambda} \leq \mathrm{TKE}_t$, indicating that due to the sampling frequency limitations of wind speed measurement instruments, the kinetic energy of turbulent eddies with frequencies between the sampling frequency and the dissipation-scale frequency cannot be captured. This leads to a theoretical underestimation of turbulent kinetic energy when derived from wind speed time series through the turbulent energy spectrum method. On the other hand, according to Equations 2a and 2b, the lower the sampling frequency $\lambda$, the greater the underestimation of $\mathrm{TKE}_{\mathrm{obs},\lambda}$ compared to $\mathrm{TKE}_t$.

According to Kolmogorov's theory, the turbulent energy spectrum $E(k)$ and the wavenumber $k$ follow the $-5/3$ power law, which is expressed as:

$$E(k) = C\varepsilon^{\frac{2}{3}}k^{-\frac{5}{3}} \tag{3}$$

where $C$ is the Kolmogorov constant, $\varepsilon$ is the turbulent dissipation rate, and $k$ is the wavenumber.

By substituting Equation 3 into Equations 2a and 2b, the relationship between $\mathrm{TKE}_{\mathrm{obs},\lambda}$ and $\mathrm{TKE}_t$ can be obtained. Thus, based on observed fluctuating wind speeds at a given sampling frequency, the TKE within the high-frequency range, from the low sampling frequency to the dissipation frequency, can be estimated through the $-5/3$ power law, enabling the calculation of $\mathrm{TKE}_t$.

### 2.4. Correction the Missed High-Frequency Turbulence by Sampling Cutoff Frequency in Observation

The High-Frequency TKE Modification Coefficient (HTMC) is defined as the ratio of TKE from unmeasured high-frequency atmospheric turbulent eddies, due to the cutoff frequency, to the measured $\mathrm{TKE}_{\mathrm{obs},\lambda}$.

$$\mathrm{HTMC} = \frac{\mathrm{TKE}_t - \mathrm{TKE}_{\mathrm{obs},\lambda}}{\mathrm{TKE}_{\mathrm{obs},\lambda}} \tag{4}$$

where $\mathrm{TKE}_{\mathrm{obs},\lambda}$ and $\mathrm{TKE}_t$ are defined as above. Therefore, after obtaining $\mathrm{TKE}_{\mathrm{obs},\lambda}$ from wind speed observations with a specific cutoff frequency $\lambda$, $\mathrm{TKE}_t$ can theoretically be determined by multiplying $\mathrm{TKE}_{\mathrm{obs},\lambda}$ by adding the factor (1 + HTMC) for correction. To validate the feasibility of HTMC correction method and determine the values of the factor HTMC, the wind speed observational data from cup anemometers (~0.05 Hz) and high-frequency ultrasonic anemometers (~10 Hz) were obtained and applied in this study. According to Nyquist sampling law, the cut-off frequencies $\lambda$ were approximately 0.025 Hz for low frequencies ($\lambda_l$) and 5 Hz for high frequencies ($\lambda_h$), respectively.

### 2.5. Coupling the HTMC Correction Into the BouLac PBL Scheme

The BouLac PBL scheme is a 1.5-order local turbulence closure scheme based on the $k$-$l$ model (Bougeault & Lacarrere, 1989). It is widely used in mesoscale atmospheric models for the parameterization of atmospheric boundary layer turbulence. Compared to other schemes, the BouLac scheme fully accounts for the shear and buoyancy production terms of turbulence, as well as the dissipation and transport of TKE. Its fundamental equation is as follows:

$$\frac{\partial \mathrm{TKE}}{\partial t} + u \cdot \nabla \mathrm{TKE} = S + B - \varepsilon - \nabla \cdot F \tag{5}$$

where $u$ *is* the wind velocity vector, $S$ and $B$ represent the shear production and buoyancy production terms of turbulence, respectively, $\varepsilon$ is the turbulence dissipation term, and $\nabla \cdot F$ denotes the transport of TKE. This equation enables the numerical calculation of the temporal and spatial distribution of TKE and its tendencies.

In coupled mesoscale numerical models such as WRF-Chem, when the horizontal spatial resolution is around 2 km, the corresponding temporal resolution, or the model's time integration step, is approximately 20 s. This indicates that the sampling cutoff frequency for wind speed data used in calculating the various terms in Equation 5 is around 0.05 Hz. Therefore, this study attempted to apply the HTMC correction.

Through the analysis of the homogeneous analytical solution of Equation 5 (shown in Text S2 in Supporting Information S1), we find that the shear production term $S$ and the buoyancy production term $B$ primarily dominate the spectral distribution characteristics of TKE. From a physical perspective, $S$ and $B$ represent the turbulence generation terms, and the frequency distribution driven by these two factors determines the final frequency distribution of TKE. Thus, in this study, both terms are multiplied by the correction factor (1 + HTMC). The modified BouLac equation is expressed as:

$$\frac{\partial \mathrm{TKE}}{\partial t} + u \cdot \nabla \mathrm{TKE} = (1 + \mathbf{HTMC}) \cdot S + (1 + \mathbf{HTMC}) \cdot B - \varepsilon - \nabla \cdot F \tag{6}$$

where HTMC is defined as in Equation 4.

After applying the HTMC correction, the BouLac scheme recalculates TKE, and the $K_m$, which governed the transport of momentum, heat, and water vapor in the atmosphere, is subsequently calculated as follows (Bougeault & Lacarrere, 1989):

$$K_m = c_k l_k \sqrt{\mathrm{TKE}} \tag{7}$$

where $l_k$ is the characteristic length scale for calculating the turbulent diffusion coefficient, and $C_k$ is a constant typically set to 0.4. The corrected $K_m$ is further incorporated into the mesoscale atmospheric chemistry model WRF-Chem. Numerical sensitivity experiments were designed to evaluate improvements in simulating the spatiotemporal distribution of near-surface atmospheric pollutant concentrations after applying the HTMC correction.

It should be emphasized that for key parameters in Equation 5 (e.g., the sampling cutoff frequency), a physically self-consistent approach would require dynamic determination based on wind speed, model spatiotemporal resolution, and TKE scaling characteristics to generate corrected TKE fields. Critically, such a design must ensure physical coherence in TKE results when simulating identical cases at varying resolutions through self-adaptive parameterization.

The current HTMC scheme fixes the sampling cutoff frequency at about 0.05 Hz. While this represents a compromise relative to the idealized framework above, it is justified by two operational imperatives: (a) Observational compatibility: This value aligns with the sampling capacity of industry-standard anemometers (e.g., MetOne 010C), ensuring consistency with historical validation data sets; (b) Practical viability: Fixed parameters preserve the portability and computational efficiency of established mesoscale parameterizations, circumventing complexities induced by dynamic scaling.

### 2.6. Initialization of Numerical Sensitivity Experiments

Winter is the season with the most frequent and severe air pollution events in Northeast China (B. Li et al., 2020), and the turbulence under the atmospheric boundary layer is often significantly underestimated, especially in winter, leading to overestimated pollutant concentrations in model simulations (Jia & Zhang, 2021). Therefore, this study focuses on a heavy haze event that occurred in November 2018 in the Shenyang metropolitan area in Northeast China, which is one of the regions where industrialization and urbanization began early. The area has long faced severe air pollution, particularly during the winter heating period when pollution levels are especially high (B. Li et al., 2020; Liu et al., 2020; Zhang et al., 2020). Additionally, the frequent regional transport of pollutants between Shenyang and neighboring cities such as Harbin, Changchun, Fushun, and Anshan, causes more severe air pollution in the region (B. Li et al., 2020; C. Li et al., 2020). Numerical sensitivity experiments were conducted to validate the improvement of HTMC correction in simulating TKE, $K_m$, and the vertical distribution characteristics of near-surface urban air pollutants.

In this study, the mesoscale atmospheric chemistry model WRF-Chem V4.3.2 was employed to simulate the period from 5 to 17 November 2018. The main analysis period of this paper is from 7 to 17 November 2018. The 48-hr spin-up period was designed for model initialization. The geographical boundaries of the simulation domain are shown in Figure 1, covering the plain region where the Shenyang urban agglomeration is located, as well as most of the surrounding hilly and mountainous areas. During this period, a heavy haze pollution event occurred in the region. A three-level nested grid configuration was applied in the model, with horizontal resolutions of 32, 8, and 2 km from the outer to the inner domain. The initial and boundary conditions were obtained from the Final Operational Global Analysis (FNL) data provided by the National Centers for Environmental Prediction (NCEP), with a spatial resolution of $1° \times 1°$. And the input data sets for land cover and topography were obtained from the official WRF (https://www2.mmm.ucar.edu/wrf/users/down-load/get_sources_wps_g-eog.html).

To evaluate the impact of introducing HTMC correction into the turbulence parameterization scheme on the simulation of vertical transport and concentration distribution of urban near-surface pollutants, two simulation groups were designed for sensitivity experiments: the control group (CTR) and the experimental group (EXP). The CTR group employed the original BouLac PBL scheme provided in WRF, while the EXP group applied the Improved BouLac PBL scheme with HTMC correction. All other physical and chemical parameterization

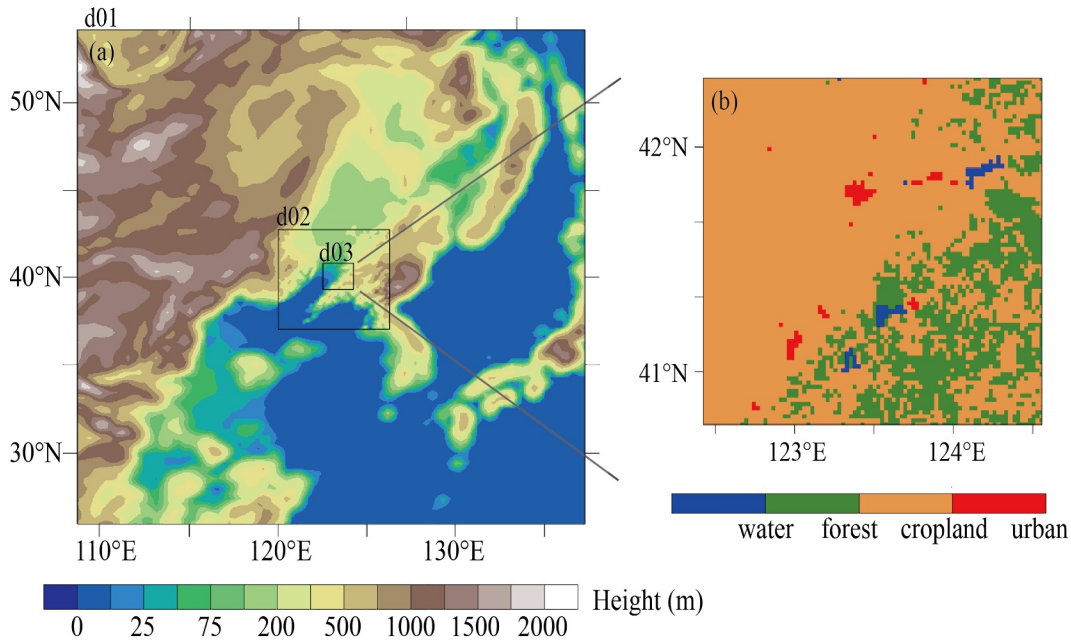


**Figure 1.** The simulation area setting in this study.

schemes were kept consistent between the two groups, as detailed in Table 1. The urban canopy model applied in this study was the multi-scale urban canopy model (MSUCM). Detailed information on the MSUCM model can be found in Z. Liu et al. (2023).

## 3. Results and Discussion

### 3.1. The Influence of the Sampling Frequency on the Turbulent Energy Spectrum

Figure 2 shows the turbulence energy spectrums of the wind speed components *u*, *v*, and *w* observed at the height of 140 m on the Beijing 325-m meteorological tower, obtained through Fourier transformation of the time series data. The red and blue lines represent high-frequency sampling data (from an ultrasonic anemometer) and low-frequency sampling data (from a cup anemometer), respectively. Figures 2a–2c display the average turbulence

**Table 1**
*The Parameterization Schemes List in the WRF-Chem Sensitivity Simulations in This Study*

| Parameterization scheme | CTR | EXP |
|---|---|---|
| Gas phase chemistry | RADM2 | |
| Microphysics | Lin | |
| Urban Canopy Model | MSUCM (Liu, Chen, et al., 2023) | |
| Cumulus physics | Grell 3D | |
| Longwave radiation | RRTMG | |
| Shortwave radiation | RRTMG | |
| Surface Layer | MM5 | |
| Planetary boundary layer | **BouLac (Bougeault & Lacarrere, 1989)** | **Improved BouLac** |
| Anthropogenic emissions | MEIC | |
| Biogenic emissions | Megan | |
| Biomass burning emissions | FINN | |
| Aerosol | RADM2/SORGAM | |

*Note*. The main difference between EXP and CTR is in bold.

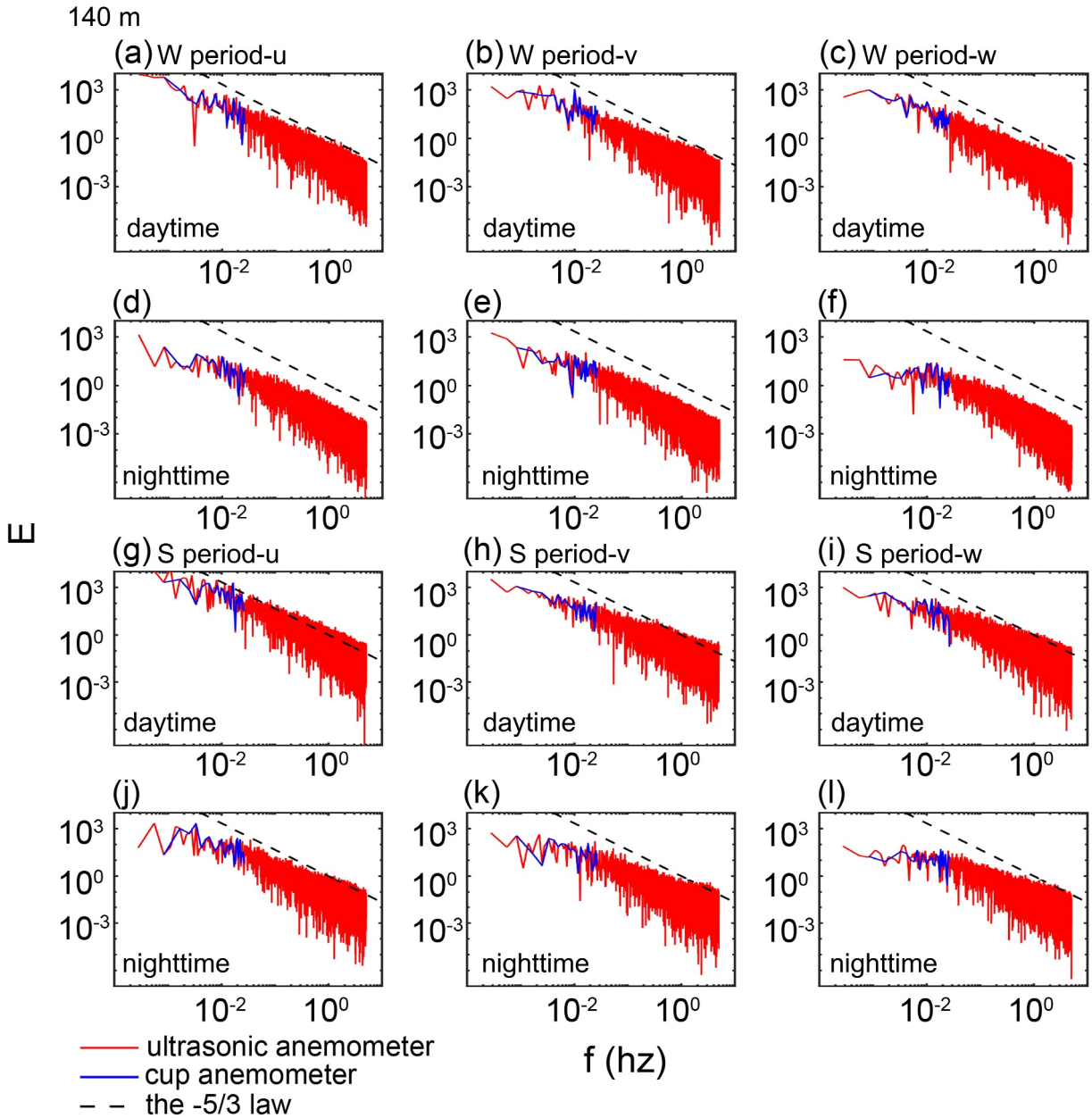


**Figure 2.** Turbulent energy spectrums of the wind speed components *u*, *v*, and *w* at 140 m height based on data from a 3D ultrasonic anemometer (red) and a cup anemometer (blue). (a–c) Show the average spectra of *u*, *v*, and *w* from 14:00–15:00 LT during W period; (d–f) from 02:00–03:00 LT during S period; (g–i) from 14:00–15:00 LT during W period; and (j–l) from 02:00–03:00 LT during S period. The black dashed lines indicate the reference slope of −5/3 from the atmospheric turbulence energy spectrum power law theory.

energy spectrums of *u*, *v*, and *w* during the daytime (14:00–15:00 LT) during the W period, while Figures 2g–2i show the corresponding energy spectrums for the same period during the S period. Figures 2d–2f present the energy spectrums during the nighttime (02:00–03:00 LT) during the W period, and Figures 2j–2l represent the nighttime spectrums for S period. The black dashed lines indicate the reference slope of −5/3 from the atmospheric turbulence energy spectrum power law theory. As shown in the figure, turbulence energy spectrums obtained from both sampling frequencies generally follow the −5/3 power-law distribution. This suggests that the turbulent eddies generated at relatively large initial scales—by either shear or buoyancy forcing mechanisms within the urban canyon—underwent a sufficiently developed cascade process consistent with the −5/3 law. However, compared to the low-frequency energy spectrums, the high-frequency energy spectrums exhibit the

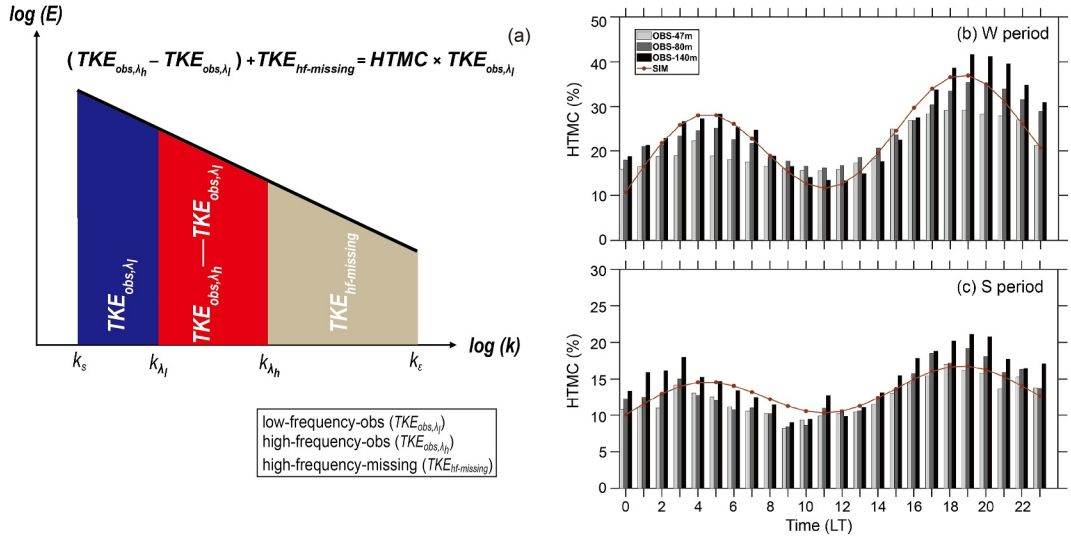


**Figure 3.** (a) Schematic of the contribution of turbulent eddies with different cutoff scales to the theoretical total turbulence energy spectrum. (b, c) Show the temporal variations of HTMC during the W and S periods, respectively, along with the parameterized HTMC. Bars from light to dark represent HTMC values at 47, 80, and 140 m, while the brown dashed line indicates the parameterized HTMC value.

cutoff frequency positioned further to the right, capturing wind speed fluctuations generated by turbulent structures with higher temporal frequencies and finer spatial scales. Additionally, the distribution of the turbulence energy spectrum varies across different seasons and times of day. Specifically, the energy values at the same frequency are higher during the daytime than at night and higher during S period than the W period at the same time of day. This indicates that, overall, atmospheric turbulence is more active during the day compared to the night and more active in summer compared to winter. These differences influence the values of $TKE_{obs,\lambda}$.

Figures S1 and S2 in Supporting Information S1 present the comparisons of high-frequency and low-frequency turbulence energy spectrums at two additional heights on the tower, 47 and 80 m, respectively. By comparing these results, it can be concluded that the turbulence spectrums at the three different heights (47 m, 80 m, and 140 m) exhibit similar distribution characteristics and numerical ranges. This similarity may be attributed to the fact that these heights are all within the urban street canyon wind environment, where the differences relevant to the focus of this study are not particularly significant.

The results in Figure 2 proved that different wind speed sampling cutoff frequencies lead to variations in the observable wavenumber range of the turbulence energy spectrum. As a result, the calculation of $TKE_{obs,\lambda}$ based on Equation 2b, varies with the different cutoff frequency. Specifically, the lower the cutoff frequency, corresponding to lower sampling frequencies of the observation instruments, the lower the calculated $TKE_{obs,\lambda}$ values.

Figure 3a illustrates the relationship between $TKE_{obs,\lambda}$ derived from wind speed data with different sampling frequencies and the theoretical $TKE_t$. The area of the blue block represents the $TKE_{obs,\lambda l}$ obtained from low-frequency sampling, which in this study corresponds to data collected by cup anemometers. The combined areas of the red and blue blocks indicate the $TKE_{obs,\lambda h}$ obtained from the three-dimensional ultrasonic anemometers, which include higher frequency and finer-scale turbulent fluctuations not detected by the cup anemometers. However, both measurement methods fail to capture the $TKE_{hf\text{-}missing}$ represented by the brown block on the right side of Figure 3a. This brown area corresponds to the turbulence energy contained in even smaller eddies, spanning from the high sampling frequency of the ultrasonic anemometer to the turbulence dissipation frequency. The combined areas of the blue, red, and gray blocks represent the theoretical $TKE_t$, as defined by Equation 2a.

Based on the −5/3 power law of the turbulence energy spectrum, the value of HTMC, as defined in Equation 4, can be derived using the quantitative relationship of $E(k)$ within the wavenumber range covered by instrument observations, represented by the red or the combined red and blue areas in Figure 3a, along with the relationships among $k_t$, $k_{\lambda l}$, $k_{\lambda h}$, and $k_\varepsilon$. The HTMC was then applied to correct $TKE_{obs,\lambda}$, and finally $TKE_t$ was obtained.

Following this method, the diurnal hourly variation of HTMC values for three sampling heights during both the W period and S period were calculated in this study. These variations are shown in Figures 3b and 3c, respectively. The height of each bar represents the multi-day average HTMC for the same hour within the corresponding month. The colors from light to dark represent the HTMC values of 47 m, 80 m, and 140 m heights, respectively. Since many related studies commonly calculate TKE based on wind speed observations from conventional meteorological data, the HTMC values presented here were derived from low-frequency observations of $TKE_{obs,\lambda l}$.

The diurnal variation of HTMC, as shown in Figures 3b and 3c, exhibits a distinct bimodal pattern. The first peak of HTMC occurs during the early morning between 3:00 and 6:00 LT, with an average value of approximately 25% at the three observed heights during the W period and around 15% during the S period. The second peak appears in the evening between 18:00 and 20:00 LT, significantly higher than the first, reaching about 37% during the W period and 20% during the S period. Overall, HTMC values are generally higher at night compared to daytime, with the lowest values, around 10%–15%, observed near noon. The bimodal feature is more pronounced during the W period, and HTMC values consistently exceed those during the S period. This indicates that the most significant underestimation of $TKE_t$ occurs during nighttime and winter. This phenomenon may be attributed to stronger atmospheric inversions and weaker large-scale or low-frequency turbulence during these times, leading to a higher contribution of small-scale or high-frequency eddies to $TKE_t$. During the early morning and evening periods, the atmospheric boundary layer tends to be more stable or in transition, and turbulence structures become more complex, with enhanced small-scale eddy activity. It may result in a greater proportion of high-frequency turbulence being missed by low-frequency sampling, thus increasing HTMC. In contrast, around midday, when the atmosphere is more convectively unstable and turbulence is dominated by larger eddies, the proportion of high-frequency TKE is relatively lower, resulting in smaller HTMC values.

Moreover, HTMC exhibits an increasing trend with height across all time periods, which could be attributed to more fully developed atmospheric turbulence and a more significant energy cascade effect with increasing altitude, influenced by the spatial distribution of the urban canopy around the observation site and the observed height range. However, as HTMC is significantly characterized by diurnal and seasonal variations, Julian day and hour were selected as independent variables to reflect its characteristics.

Based on the results in Figure 3, a correction function of HTMC diurnal variation and its seasonal differences were obtained by fitting analysis. The correction function will be used for the adjustment from $TKE_{obs,\lambda l}$ to $TKE_t$. The expression of the correction function is given as follows:

$$\mathrm{HTMC} = \left(1 + 0.01 * \left(5 \sin\left(\frac{\pi}{12}\left(\mathrm{LT} - \frac{\pi}{6}\right)\right)\cos\left(\frac{\pi}{19}\mathrm{LT}\right) + 1\right)\left(0.9 \cos\left(\left(\mathrm{Julian} - \frac{\pi}{2}\right)\frac{2\pi}{365}\right) + 1.4\right) + 0.05\right)^2 - 1 \tag{8}$$

where Julian represents the Julian day, used to characterize the seasonal variation of HTMC, while LT denotes the local true solar time, reflecting the diurnal variation of HTMC.

In Figures 3b and 3c, the brown dashed lines represent the average diurnal variation curves of HTMC during the W period and S period, as derived from Equation 8. The figures show that this parameterization scheme well captures the observed bimodal diurnal variation of HTMC, as well as the seasonal pattern of higher values in winter and lower values in summer. The HTMC reaches its minimum around 11:00 LT during the daytime, approximately 13% in winter and 10% in summer, and peaks around 19:00 LT at night, with about 37% in winter and roughly half of that in summer, around 17%. This fitting result reasonably reflects the variations and characteristics of HTMC from observations. Although studies by Obukhov (1971) and Zilitinkevich et al. (2013) have demonstrated that the cascade processes in atmospheric turbulence can be more complex, for instance, buoyant production of TKE may induce an inverse cascade from smaller to larger scales, the turbulence energy spectra observed in urban street canyons (as shown in Figure 2, Figures S1and S2 in Supporting Information S1) still exhibit good agreement with the −5/3 power law. Therefore, the HTMC scheme proposed in this study remains broadly applicable under most conditions.

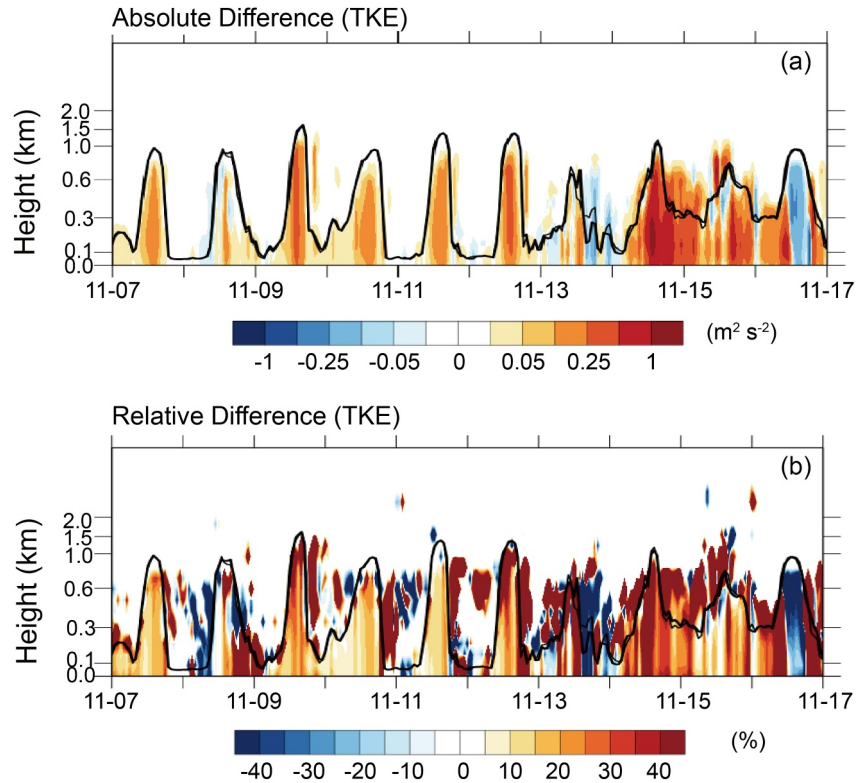


**Figure 4.** The differences in the vertical distribution of TKE over urban Shenyang between the EXP group and CTR group. (a) Shows the absolute difference, and (b) shows the relative difference. Color shading represents the TKE differences, with warm colors indicating higher TKE simulation values in the EXP group compared to the CTR, and cool colors indicating the opposite.

### 3.2. Validation of HTMC Correction on the Simulated $TKE_t$ and $K_m$

In this study, the HTMC was further incorporated into the BouLac PBL scheme in WRF-Chem, forming the Improved BouLac PBL scheme. The modified mathematical model is presented in Equations 6 and 7. Subsequently, sensitivity numerical experiments were conducted to simulate the spatiotemporal distributions of near-surface atmospheric turbulence, atmospheric diffusion coefficient, and atmospheric pollutant concentrations during a severe haze event in Shenyang and its surrounding areas in China.

Figure 4 shows the differences in the simulated vertical distribution of TKE over urban Shenyang between the EXP group and CTR group. Figure 4a represents the absolute difference, while Figure 4b shows the relative difference. The differences are represented by color shading, with warm colors indicating higher TKE simulation values in the EXP group compared to the CTR, and cool colors indicating the opposite. As shown in Figure 4a, during most periods, the TKE below the top of the atmospheric boundary layer in the EXP group was higher than that in the CTR group. During daytime, the TKE increased by 0.1–1 $m^2\ s^{-2}$, while at night, the increase ranged from 0.01 to 0.25 $m^2\ s^{-2}$, indicating that the TKE enhancement was more pronounced during the day than at night. However, some periods showed the opposite trend, which may be attributed to complex surrounding transport processes influenced by increased vertical turbulence in specific spatiotemporal regions, considered occasional phenomena. The negative difference only occurred during a few hours, indicating that the HTMC correction was not a simple correction but rather a more accurate reflection of the actual turbulent processes overall. Overall, after applying the HTMC correction, the absolute intensity of the simulated near-surface TKE has significantly increased.

Figure 4b shows that the relative difference of TKE generally ranged between 10% and 40%. During the daytime, the relative difference was around 10%–20%, while at night it reached as high as 20%–40%. This diurnal pattern aligned with the temporal variation of the HTMC shown in Figure 3, indicating that the HTMC correction was appropriately applied in the EXP simulation results. Further, when compared with Figure 4a, it is observed that

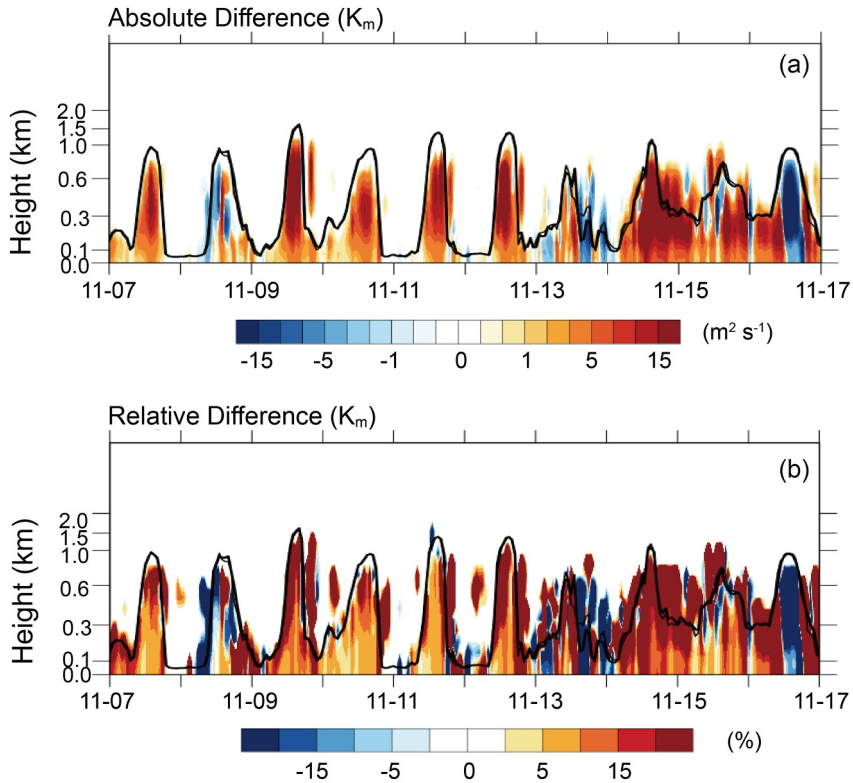


**Figure 5.** The differences in the vertical distribution of $K_m$ over urban Shenyang between the EXP group and CTR group. (a) Shows the absolute difference, and (b) shows the relative difference. Color shading represents the $K_m$ differences, with warm colors indicating higher $K_m$ simulation values in the EXP group compared to the CTR, and cool colors indicating the opposite.

although the absolute difference between EXP and CTR was higher during the day and lower at night, the relative difference exhibited the opposite trend, being higher at night and lower during the day. This phenomenon can be explained as follows: On one hand, the overall intensity of atmospheric turbulence is stronger during the day due to solar radiation heating the surface, which leads to stronger thermal convection and buoyancy-driven turbulence. Additionally, higher average wind speeds during the day generate stronger wind shear and mechanically driven turbulence, which, through the turbulence energy cascade effect, produces more high-frequency turbulence that carries greater TKE. On the other hand, nighttime turbulence activity is weaker, mainly characterized by a significant reduction in large-scale, low-frequency turbulence eddies. Consequently, the relative contribution of high-frequency turbulent energy increases. This could also explain why most current models tend to underestimate nighttime TKE and $K_m$.

According to Equation 7, the simulated TKE in the model further influences the spatiotemporal distribution of atmospheric turbulent diffusion coefficients. Figure 5 shows the differences in the vertical distribution of $K_m$ over Shenyang between the EXP and CTR groups, with (a) representing absolute difference and (b) representing relative difference. Warm colors indicate higher diffusion coefficients in the EXP compared to the CTR, while cool colors indicate the opposite. As shown in Figure 5a, similar to TKE, the $K_m$ below the atmospheric boundary layer was generally higher in the EXP at most times. TKE determines $K_m$, so the moment when $K_m$ was lower in the EXP was consistent with the time when TKE was lower, but the negative difference only existed for a few hours. It shows that HTMC correction is not a simple correction but rather a more accurate reflection of the turbulent processes overall. During the daytime, $K_m$ in the EXP increased by 5–15 $m^2$ $s^{-1}$, while at night, the increase ranged from 1 to 5 $m^2$ $s^{-1}$, indicating that the magnitude of the increase was greater during the day. After applying the HTMC correction, the absolute magnitude of the $K_m$ was significantly enhanced overall. The deviation pattern of $K_m$ between the EXP and CTR was consistent with that of TKE in both simulations, further confirming that TKE determines the diffusion coefficient.

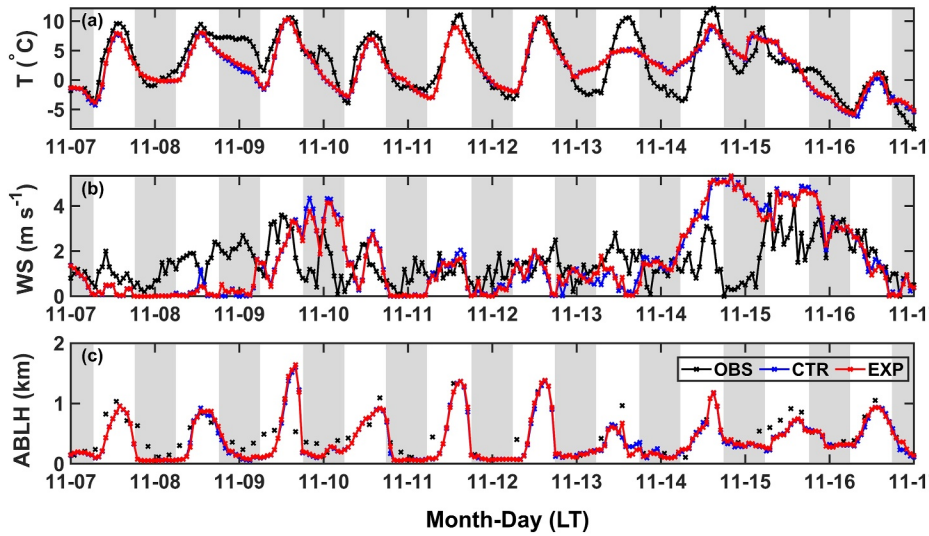


**Figure 6.** Time series of near-surface meteorological conditions over urban Shenyang. The black dots represent observed value, while the red and blue dots indicate simulated concentrations in the EXP and CTR groups, respectively. Shaded areas denote nighttime periods, and the white areas denote daytime periods.

Figure 5b shows that the relative difference of $K_m$ in two groups generally ranged from 10% to 20%, with positive deviations of 10%–15% during the daytime and up to 15%–20% at night. Combined with Figure 4, it is evident that the improvements in $K_m$ in the EXP compared to the CTR exhibit similar characteristics to those of TKE: higher absolute difference during the day and lower at night, while relative difference was lower during the day and higher at night. These results indicate that during nighttime, when atmospheric turbulence is relatively weak, high-frequency turbulence contributes more significantly to the relative proportion of the diffusion coefficient.

### 3.3. Validation of HTMC Correction on the Simulated Meteorological Conditions

Figure 6 shows the time series of the near-surface meteorological conditions in the Shenyang urban area, including (a) near-surface temperature (T), (b) wind speed (WS) and (c) atmospheric boundary layer height (ABLH). The black dots represent the observed values, and the red and blue dots represent the simulated values of the EXP and CTR groups, respectively. Figure 6a shows that near-surface air temperature in urban Shenyang exhibited a typical diurnal cycle during the study period, with higher temperatures during the day and lower temperatures at night. The daily maximum temperature generally exceeded 10°C, reaching the highest value of 12°C at 13:00–14:00 LT on November 14. In contrast, the daily minimum temperature mostly remained between −5°C and −3°C, with the lowest value recorded at 00:00 LT on November 17. Both the CTR and EXP reproduced the magnitude and diurnal pattern of the near-surface temperature reasonably well. However, the EXP consistently produced higher nighttime temperatures than the CTR, especially during the early hours of November 7, 9, and 16, when the temperature simulated by EXP exceeded that of CTR by more than 0.5°C. Comparison with observations indicates that CTR significantly underestimated nighttime temperatures during these periods, reflecting a deficiency in capturing the urban canyon heat storage effect at night, whereas EXP aligned more closely with the observations. This improvement is likely attributable to the enhanced TKE and $K_m$ in EXP, which facilitated the downward transport of warm air from aloft, thereby slowing the nocturnal surface cooling and better representing the underlying physical processes. Additionally, the EXP also simulated slightly higher daytime maximum temperatures compared to CTR, particularly on the afternoons of November 7, 8, 14, and 16, which were also more consistent with observations. This indicates that the enhanced turbulence in the EXP strengthened vertical heat mixing in urban areas during the day, and, when combined with improved nighttime heat storage effect, resulted in a better overall agreement with observed near-surface temperature.

Figure S3 in Supporting Information S1 presents a scatter plot of the simulation and observation of the near-surface temperature (T). The $X$ value of each scatter point stands for the observed T, while the $Y$ value stands for the simulated T. Red dots indicate the results from the EXP, with the red solid line representing the linear fitting line for the EXP. Similarly, blue dots and the blue solid line represent the corresponding results for the

**Table 2**
*Simulation Bias Evaluation of Key Meteorological Variables*

| | NMB (%) | | NME (%) | | RMSE | | $r$ | |
|---|---|---|---|---|---|---|---|---|
| Variables | CTR | EXP | CTR | EXP | CTR | EXP | CTR | EXP |
| T (daytime) | −0.24 | −0.20 | 0.37 | 0.35 | 0.19 | 0.19 | 0.88 | 0.88 |
| T (nighttime) | −0.17 | **0.04** | 3.54 | **3.47** | 0.30 | **0.29** | 0.69 | **0.71** |
| WS (daytime) | −0.01 | −0.02 | 0.68 | 0.67 | 0.33 | 0.32 | 0.35 | 0.36 |
| WS (nighttime) | 0.19 | 0.18 | 0.93 | 0.89 | 0.47 | 0.46 | 0.24 | 0.25 |
| ABLH (daytime) | −0.17 | −0.15 | 0.33 | 0.31 | 0.23 | 0.23 | 0.69 | 0.70 |
| ABLH (nighttime) | −0.33 | **−0.28** | 0.35 | **0.32** | 0.25 | **0.23** | 0.60 | **0.61** |

*Note*. The variables with better performance and pass the two-sample Student's $t$-test of significance are in bold. Normalized Mean Bias (NMB): $\mathrm{NMB} = \frac{\sum_1^N (S_i - O_i)}{\sum_1^N O_i} \times 100\%$. Normalized Mean Error (NME): $\mathrm{NME} = \frac{\sum_1^N |S_i - O_i|}{\sum_1^N O_i} \times 100\%$. Root Mean Square Error (RMSE): $\mathrm{RMSE} = \sqrt{\frac{\sum_1^N \left(\frac{S_i - O_i}{O_i}\right)^2}{N}}$. Correlation Coefficient ($r$): $r = \frac{\sum (S_i - \overline{S}) \sum (O_i - \overline{O})}{\sqrt{\sum (S_i - \overline{S})^2 \sum (O_i - \overline{O})^2}}$, where $Si$ and $Oi$ represent the simulated value and the observed value of a variable, respectively, while $\overline{S}$ and $\overline{O}$ represent the mean value of the simulation and observation of the variable, respectively, and $N$ indicates the number of the variable.

CTR. The closer the scatter points are to the $y = x$ reference line (the black dashed line), the better the agreement between the simulated and observed values. The scatter plot is based on the same data set as Figure 6a but separates the data into daytime and nighttime periods according to local time. Figure S3a in Supporting Information S1 shows the results for the daytime period (7:00–18:00 LT), while Figure S3b in Supporting Information S1 represents the nighttime period (19:00–6:00 (day + 1) LT). During the daytime, the observed T ranged from −5 to 13°C. The simulated values from both groups generally agreed well with the observations, as indicated by the relatively uniform distribution of scatter points around the $y = x$ line and the similar slopes of the fitting lines for the two simulations. In contrast, during the nighttime period, temperatures ranged from −10 to 8°C, and the slope of the fitting line for the EXP was 0.02 higher than that of the CTR, indicating a closer alignment with the reference line.

Table 2 summarizes the bias statistical indicators for the near-surface meteorological conditions during the study period, quantifying the deviations between the simulated values from the two simulation groups and the observed data. The Normalized Mean Bias (NMB) reflects the average values and direction of the bias, while the Normalized Mean Error (NME) represents the normalized mean of the absolute deviations. The Root Mean Square Error (RMSE) indicates the statistical variance of the normalized deviations between the simulated and observed values, and the correlation coefficient ($r$) indicates the correlation between the simulations and observations. For each variable, when the difference between the simulated and observed values passes the two-sample Student's $t$-test and the statistical indicator is smaller compared to the other group, the indicator is highlighted in bold. During the daytime period, the EXP shows a modest improvement in simulation performance compared to the CTR, with NMB reduced from −0.24 to −0.20 and NME from 0.37 to 0.35. The improvement is more pronounced during nighttime, where the NMB in the EXP decreased significantly from −0.17 to 0.04, and NME was reduced from 3.54 to 3.47. Meanwhile, the correlation coefficient $r$ increased from 0.69 to 0.71. In addition, the difference between the two simulation groups during the nighttime passed the significance test, indicating that the improvement in nighttime near-surface T in the EXP is statistically significant.

Figure 6b presents the time series of near-surface wind speed over urban Shenyang during the same period. Compared to the T, WS exhibited a less distinct diurnal cycle, though it generally remained higher during the daytime than at night. The differences in simulated WS between the two groups were relatively minor. Figure S4 in Supporting Information S1, which provides a corresponding scatter plot, further supports this conclusion—both groups showed similar fitting line slopes for daytime and nighttime periods, indicating minimal differences in simulation performance. Consistently, the statistical indicators in Table 2 show that although the EXP exhibits slightly reduced bias during the nighttime, the differences between the two simulations do not pass the significance test, suggesting that this improvement was not statistically significant.

Figure 6c illustrates the time series of atmospheric boundary layer height (ABLH). Observational data show that ABLH remained around 0.2 km at night and increased to above 1 km during the daytime. Both simulation groups reproduced this diurnal variation pattern, though the absolute values were generally underestimated. Compared with the CTR, the ABLH simulated by EXP was slightly higher in most periods, especially during the afternoon to nighttime hours of November 8–9 and November 14–16, where the ABLH increased by approximately 50–150 m, causing the results closer to observations. When combined with the patterns of TKE and $K_m$ shown in Figures 4 and 5, as well as the near-surface T results in Figure 6a, it further demonstrates that the enhanced TKE and $K_m$ in the EXP contribute to improved simulation accuracy of near-surface temperature and ABLH in urban areas, making them more consistent with observational data.

The scatter plots in Figure S5 in Supporting Information S1 further confirm the reliability of the simulation results. It is based on the same data set as Figure 6c but separates the data into daytime and nighttime periods according to local time. During the daytime period, both groups exhibited good agreement with observations, with

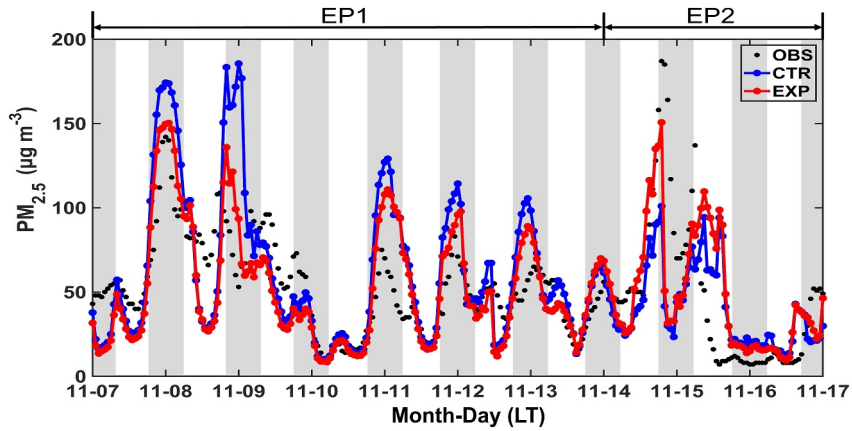


**Figure 7.** Time series of $PM_{2.5}$ concentrations over urban Shenyang. The black dots represent observed near-surface concentration, while the red and blue dots indicate simulated concentrations in the EXP and CTR groups, respectively. Shaded areas denote nighttime periods, and the white areas denote daytime periods.

fitting line slopes of 0.93 for the CTR and 0.95 for the EXP, indicating a slight improvement in the EXP. The statistical metrics also show slightly reduced biases for the EXP. The improvement was more evident during the nighttime: the fitting line slope increased from 0.57 to 0.61, NMB decreased from −0.33 to −0.28, NME dropped from 0.35 to 0.32, RMSE decreased from 0.25 to 0.23, and $r$ increased from 0.60 to 0.61. Moreover, these improvements passed the significance test, indicating that the enhancement of EXP in simulating nighttime ABLH was statistically significant.

In summary, the meteorological variables near-surface air temperature, wind speed, and boundary-layer heights show markedly smaller differences between CTR and EXP than TKE and $K_m$.

We attribute the limited improvements in meteorological variables to the following mechanisms: For the near-surface air temperature, mechanically driven turbulence from buildings/vegetation maintains predominantly neutral potential temperature profiles in urban street canyons. This persistence (evident in Figure 6a) minimizes thermal gradient and energy flux changes regardless of HTMC implementation. Only during the nighttime does radiative cooling facilitate stable boundary layers, where HTMC may enhance TKE and partially mitigate the existence of near-ground stable boundary layers, yielding discernible temperature differences (as shown in Figure 6a).

For meso-scale grid averaged wind speed and ABLH, HTMC primarily corrects subgrid-scale turbulent eddies, with spatiotemporal scales of far lower than 2 km in horizontal resolution. Their velocity fluctuations undergo statistical cancellation during grid averaging, thus failing to drive systematic variations in resolved wind speed or boundary-layer depth.

Afterall, the enhanced TKE and $K_m$ in the EXP still improved the simulation performance of meteorological variables. This improvement was particularly evident during the nighttime period, when the relative increase in TKE and $K_m$ were more pronounced. The strengthened vertical thermodynamic exchange effectively enhanced the simulation accuracy of near-surface temperature and atmospheric boundary layer height. These results show the crucial role of enhanced high-frequency turbulence characteristics in improving the model's performance to reproduce key meteorological elements, and further validate the effectiveness of the HTMC correction scheme in refining the simulation of nocturnal boundary layer processes. The associated changes in ABLH and thermodynamic conditions may have a substantial impact on the transport and dispersion of pollutants, thereby influencing the performance of air pollutant concentration simulations, which will be further discussed.

### 3.4. Validation of HTMC Correction on the Simulated Air Pollutant Concentrations

Figure 7 shows the time series of near-surface $PM_{2.5}$ concentrations over urban Shenyang. The black dots represent observed near-surface concentration, while the red and blue dots indicate simulated concentrations in the EXP and CTR groups, respectively. Shaded areas denote nighttime periods, and the white areas denote daytime periods. The observations indicated a clear diurnal pattern, with lower $PM_{2.5}$ concentrations during the

day and higher concentrations at night. Two peaks exceeding 100 μg $m^{-3}$ were primarily observed during the night of November 7 to the early morning of November 8, and from the night of November 14 to the early morning of November 15. Based on the variation characteristics of $PM_{2.5}$ concentrations, the simulation period can be divided into two pollution episodes. As shown in Figure 7, the first pollution episode (EP1) was primarily driven by local emissions, with pollutant concentrations concentrated near the surface, whereas the second pollution episode (EP2) was characterized by regional transport aloft. Therefore, the study period was separated into two episodes. EP1 occurred from November 7 to November 13, with $PM_{2.5}$ concentrations rising rapidly between November 7 and 8, peaking at midnight on November 8, and then gradually decreasing to below 15 μg $m^{-3}$ by 2:00 LT on November 10. The second pollution episode (EP2) occurred from November 14 to November 17, with the highest $PM_{2.5}$ concentration reaching 190 μg $m^{-3}$ at 8:00 LT on November 14. The comparison between the simulated and observed values shows that both simulation groups captured the general trend and diurnal variation of $PM_{2.5}$ concentrations reasonably well. However, the simulation results in EXP were closer to the observations in terms of magnitude. In EP1, the CTR exhibited a systematic overestimation of nighttime $PM_{2.5}$ concentrations, with simulated values at least 20 μg $m^{-3}$ higher than the observations. This overestimation was significantly reduced in the EXP group and the $PM_{2.5}$ concentrations were more closely aligned with the observations. In EP2, while the $PM_{2.5}$ concentrations simulated by the EXP were generally lower than the observations, they were higher than those from the CTR, especially during the night of November 14 and early morning of November 15, and demonstrated better agreement with the measurements.

Figure S6 in Supporting Information S1 presents a scatter plot of the simulation and observation of $PM_{2.5}$ concentrations. The *X* value of each scatter point stands for the observed $PM_{2.5}$ concentrations, while the Y value stands for the simulation concentrations. Red dots indicate the results from the EXP, with the red solid line representing the linear fitting line for the EXP. Similarly, blue dots and the blue solid line represent the corresponding results for the CTR. The closer the scatter points are to the $y = x$ reference line (the black dashed line), the better the agreement between the simulated and observed values. The scatter plot is based on the same data set as Figure 7 but separates the data into daytime and nighttime periods according to local time. Figure S6a in Supporting Information S1 shows the results for the daytime period (7:00–18:00 LT), while Figure S6b in Supporting Information S1 represents the nighttime period (19:00–6:00 (day + 1) LT). During the daytime, the observed $PM_{2.5}$ concentrations were relatively low, mostly ranging from 0 to 50 μg $m^{-3}$. In contrast, the nighttime data points were predominantly distributed in regions where the observed values exceed 50 μg $m^{-3}$, further confirming the diurnal pattern of lower $PM_{2.5}$ concentrations during the day and higher concentrations at night. Based on the distance of the scatter points and fitting lines from the $y = x$, it is evident that both the points and the fitting line of the EXP in Figure S6 in Supporting Information S1 were consistently closer to $y = x$ compared to the CTR. This indicates that the $PM_{2.5}$ simulations in EXP were in better agreement with the observations throughout the whole day, while the CTR tended to significantly overestimate $PM_{2.5}$ concentrations, particularly during nighttime. A further comparison reveals that the differences between the EXP and CTR were more significant during the nighttime, with the EXP results being closer to the observations. While the improvement of EXP during the daytime was small, there was still a big difference between the simulated $PM_{2.5}$ concentrations in EXP and the observed concentrations in the daytime period.

Table 3 summarizes the bias statistical indicators for major air pollutant concentrations during the pollution events, quantifying the deviations between the simulated values from the two simulation groups and the observed data. The Normalized Mean Bias (NMB) reflects the average values and direction of the bias, while the Normalized Mean Error (NME) represents the normalized mean of the absolute deviations. The Root Mean Square Error (RMSE) indicates the statistical variance of the normalized deviations between the simulated and observed values, and the correlation coefficient (*r*) indicates the correlation between the simulations and observations. For each variable, when the difference between the simulated and observed values passes the two-sample Student's *t*-test and the statistical indicator is smaller compared to the other group, the indicator is highlighted in bold. As shown in Table 3, during the daytime period, the bias statistical indicators for $PM_{2.5}$ concentrations in both simulation groups were relatively similar, and the difference between the two groups and the observed value did not pass the *t*-test, indicating no statistically significant difference in model performance between EXP and CTR. However, during the nighttime period, NMB, NME, and RMSE of $PM_{2.5}$ were all reduced by more than 30% compared to the CTR. Especially, the NMB decreased significantly from 23.77% in the CTR to 6.18% in the EXP, and the *r* improved from 0.68 to 0.75. These results clearly demonstrate that the Improved BouLac scheme has a significant improvement in simulating near-surface $PM_{2.5}$ concentrations at

**Table 3**
*Simulation Bias Evaluation of Key Environmental Variables*

| | NMB (%) | | NME (%) | | RMSE | | *r* | |
|---|---|---|---|---|---|---|---|---|
| Variables | CTR | EXP | CTR | EXP | CTR | EXP | CTR | EXP |
| $PM_{2.5}$ (daytime) | −3.09 | 2.12 | 40.35 | 42.99 | 0.13 | 0.14 | 0.60 | 0.62 |
| $PM_{2.5}$ (nighttime) | 23.77 | **6.18** | 50.58 | **35.79** | 0.27 | **0.18** | 0.68 | **0.75** |
| $NO_2$ (daytime) | −2.07 | 3.95 | 26.99 | 28.50 | 0.19 | 0.19 | 0.42 | 0.40 |
| $NO_2$ (nighttime) | 16.30 | **5.67** | 34.33 | **25.18** | 0.26 | **0.17** | 0.71 | **0.73** |

*Note*. The variables with better performance and pass the two-sample Student's *t*-test of significance are in bold. Normalized Mean Bias (NMB): $\mathrm{NMB} = \frac{\sum_1^N (S_i - O_i)}{\sum_1^N O_i} \times 100\%$. Normalized Mean Error (NME): $\mathrm{NME} = \frac{\sum_1^N |S_i - O_i|}{\sum_1^N O_i} \times 100\%$. Root Mean Square Error (RMSE): $\mathrm{RMSE} = \sqrt{\frac{\sum_1^N \left(\frac{S_i - O_i}{O_i}\right)^2}{N}}$. Correlation Coefficient (*r*): $r = \frac{\sum (S_i - \overline{S}) \sum (O_i - \overline{O})}{\sqrt{\sum (S_i - \overline{S})^2 \sum (O_i - \overline{O})^2}}$, where *Si* and *Oi* represent the simulated value and the observed value of a variable, respectively, while $\overline{S}$ and $\overline{O}$ represent the mean value of the simulation and observation of the variable, respectively, and *N* indicates the number of the variable.

night. Figure S7 in Supporting Information S1 shows the average daily variation of $PM_{2.5}$ and $NO_2$ concentration in the Shenyang urban area. The black dots are the observed values, the red dots are the simulation results of the EXP, the red shadow is the root mean square error interval of the EXP, the blue dots and the blue shadow show the corresponding results of CTR. During the pollution episode, $PM_{2.5}$ exhibited a distinct diurnal cycle, with higher concentrations at night and lower levels during the daytime. The minimum concentrations occurred around 13:00 LT each day, with enhanced atmospheric dispersion conditions. At night, average $PM_{2.5}$ concentrations reached up to 60 μg $m^{-3}$. Both the EXP and CTR simulations reproduced the general diurnal trend reasonably well. However, differences between the two schemes were minor during daytime, while the EXP reduced the overestimation of near-surface $PM_{2.5}$ concentrations in the CTR during nighttime, particularly between 20:00 and 04:00 (day + 1) LT.

These results indicate that, after applying the Improved BouLac scheme, the EXP simulated stronger atmospheric TKE and $K_m$, which subsequently led to nighttime $PM_{2.5}$ concentrations more consistent with observations. This effectively improved the significant overestimation of nighttime $PM_{2.5}$ concentrations in the CTR. Furthermore, these findings demonstrate the critical role of high-frequency TKE in simulating nighttime pollutant concentrations.

Figure 8 presents the time series of vertical profiles of $PM_{2.5}$ concentrations over urban Shenyang in (a) the EXP, (b) the CTR, and (c) the differences between the two simulation groups. In Figures 8a and 8b, the color shading represents $PM_{2.5}$ concentrations in each simulation group, with the solid black line indicating the simulated ABLH. In Figure 8c, the color shading shows the $PM_{2.5}$ concentration differences between the EXP and CTR, where warm colors indicate higher $PM_{2.5}$ concentrations in the EXP compared to the CTR, and cool colors indicate the opposite. The thinner and thicker black lines represent the ABLH in the CTR and EXP, respectively. During the first pollution episode (EP1), $PM_{2.5}$ primarily originated from local emissions. Because the vertical distribution of $PM_{2.5}$ concentrations in Figures 8a and 8b indicates that pollutants were mainly concentrated in the near-surface layer, with concentrations rapidly decreasing with height and there are no signs of elevated pollutant layers or long-range transport aloft were observed in the atmospheric boundary layer.

As shown in Figures 4 and 5, the EXP group simulated stronger atmospheric TKE and larger turbulent diffusion coefficients, which was conducive to the vertical diffusion of near-surface pollutants and enhanced their upward transport. Consequently, the EXP simulated lower $PM_{2.5}$ concentrations near the surface and higher concentrations at higher altitudes compared to the CTR. This phenomenon was particularly pronounced at night, with $PM_{2.5}$ concentration differences between the two simulations exceeding 20 μg $m^{-3}$ near the surface. The reason is that the observations in Figure 7 indicated that pollutant accumulation mainly occurred during nighttime, and the CTR significantly overestimated concentrations during these periods. The HTMC correction enhanced vertical turbulent diffusion at night in the EXP, effectively reducing near-surface accumulation. Consequently, the concentration differences between EXP and CTR were more significant during nighttime. While during the daytime, the original model already simulated relatively strong turbulent mixing, resulting in a smaller impact from HTMC and thus less pronounced differences. During the second pollution episode (EP2), pollutant transport from surrounding regions at higher altitudes was observed on November 14. The stronger turbulent diffusion in the EXP promoted the downward transport of these elevated pollutants toward the surface. As a result, Figure 8c shows higher near-surface $PM_{2.5}$ concentrations in the EXP compared to the CTR. This characteristic was consistent with the results in Figure 7, which further confirms that the $PM_{2.5}$ concentrations simulated in EXP were more consistent with observations during this period. Therefore, the diurnal contrast in Figure 8c should not be only attributed to variations in turbulent diffusion, but rather show the different effect of the high-frequency TKE under distinct pollution conditions: alleviating underestimated vertical diffusion during nighttime in EP1, and enhancing downward pollutant transport during daytime in EP2.

Figure 9 shows the vertical profiles of $PM_{2.5}$ concentrations at several typical moments during the simulation period. The black solid lines represent the observed concentrations, while the blue and red solid lines denote the

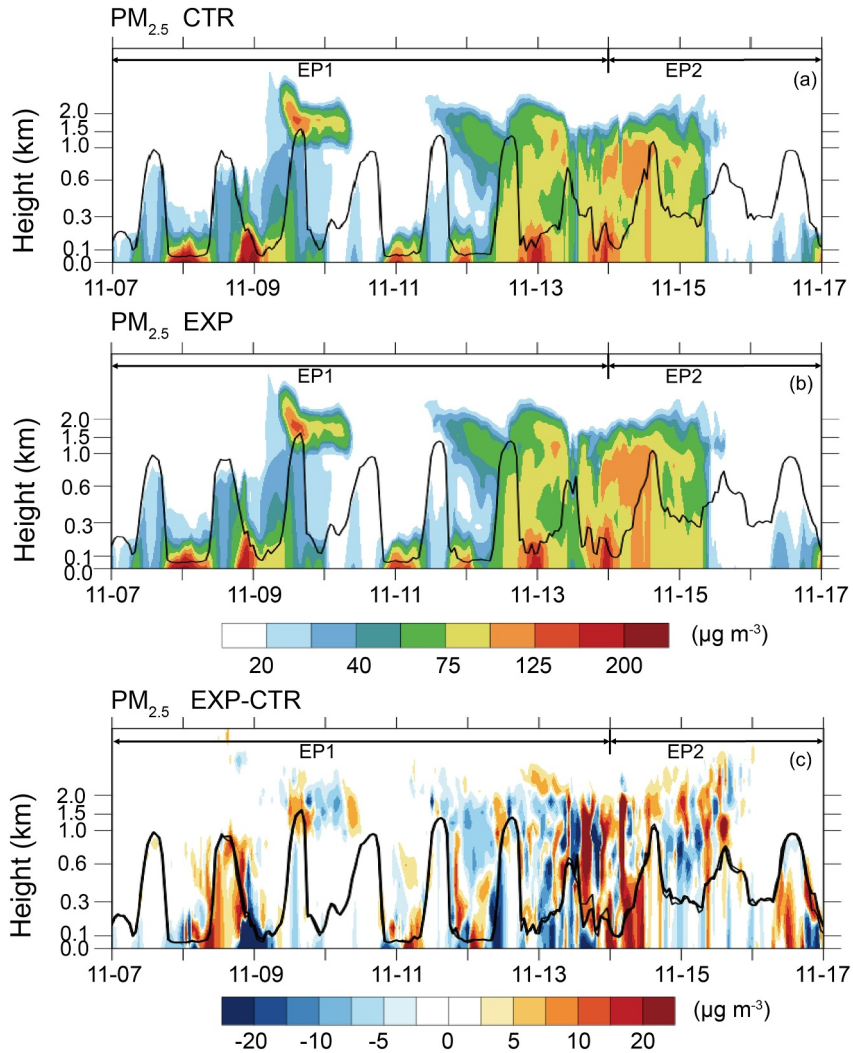


**Figure 8.** Time series of vertical profiles of $PM_{2.5}$ concentrations over urban Shenyang in (a) the EXP, (b) the CTR, and (c) the differences between the two simulation groups. The color shading in (a, b) represents $PM_{2.5}$ concentrations in each simulation group, and the black solid lines show the simulated ABLH. In (c), warm colors indicate higher $PM_{2.5}$ concentrations in EXP and cool colors indicate the opposite. The thinner and thicker black lines represent the ABLH in the CTR and EXP, respectively.

simulated concentrations in the CTR and EXP groups, respectively. Figures 9a–9d show typical moments of EP1, with Figures 9a and 9c representing nighttime and Figures 9b and 9d representing daytime. Figure 9e shows the typical moment of EP2. During EP1, the differences between the EXP and CTR were small during the daytime, with the EXP simulating slightly lower $PM_{2.5}$ concentrations than that of the CTR. Both simulation groups underestimated $PM_{2.5}$ concentrations compared to observations. However, at night, the vertical distribution of $PM_{2.5}$ concentrations below 100 m in two groups was significantly different, with lower concentrations in the EXP than the CTR and better agreement with observations. This indicates that the HTMC correction applied to TKE in the EXP enhanced vertical turbulent diffusion, reducing near-surface pollutant concentrations while increasing concentrations at higher altitudes, significantly improved the simulation of nighttime $PM_{2.5}$ concentrations. During EP2, influenced by pollutant transport from surrounding regions at higher altitudes, the stronger $K_m$ in the EXP promoted the downward transport of upper pollutants. Consequently, $PM_{2.5}$ concentrations in the EXP were higher than those in the CTR below 600 m, with the distribution more consistent with observations. Moreover, this improvement was particularly significant below 100 m, highlighting the effectiveness of the HTMC correction in simulating near-surface pollution.

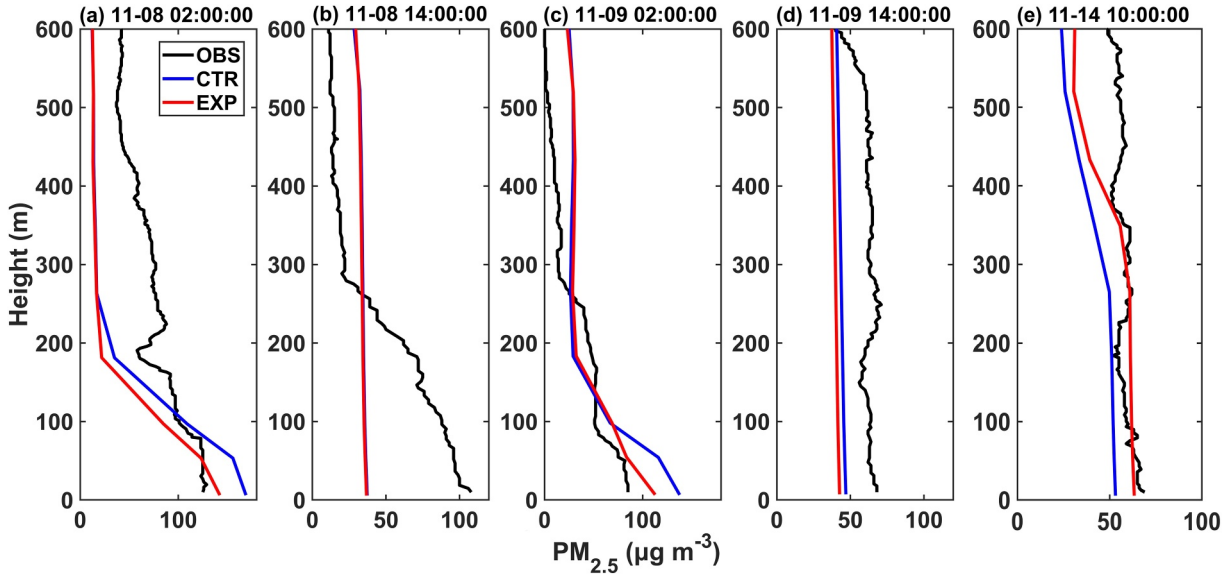


**Figure 9.** The vertical profiles of $PM_{2.5}$ concentrations at several typical moments during the simulation period. The black solid lines represent the observed concentrations, while the blue and red solid lines denote the simulated concentrations in the CTR and EXP groups, respectively.

Figure 10 shows the spatial distribution of near-surface concentration differences between the EXP and CTR groups for (a–e) $PM_{2.5}$ and (f–j) $NO_2$ at the selected typical moments. Warm colors indicate higher concentrations in EXP compared to CTR, while cool colors represent the opposite. The stars mark the location of the Shenyang urban area. Each subplot represents the average concentration difference between the two simulation groups over the current moment and the preceding and following 2 hours. The results show that concentration differences between the two simulation groups were primarily concentrated around the urban area, driven by the thermal and dynamic property differences between urban and suburban regions. After applying the HTMC correction, the difference in turbulent diffusion capacity between EXP and CTR became more pronounced within the urban region, resulting in larger pollutant concentration differences near the urban area compared to the surrounding regions.

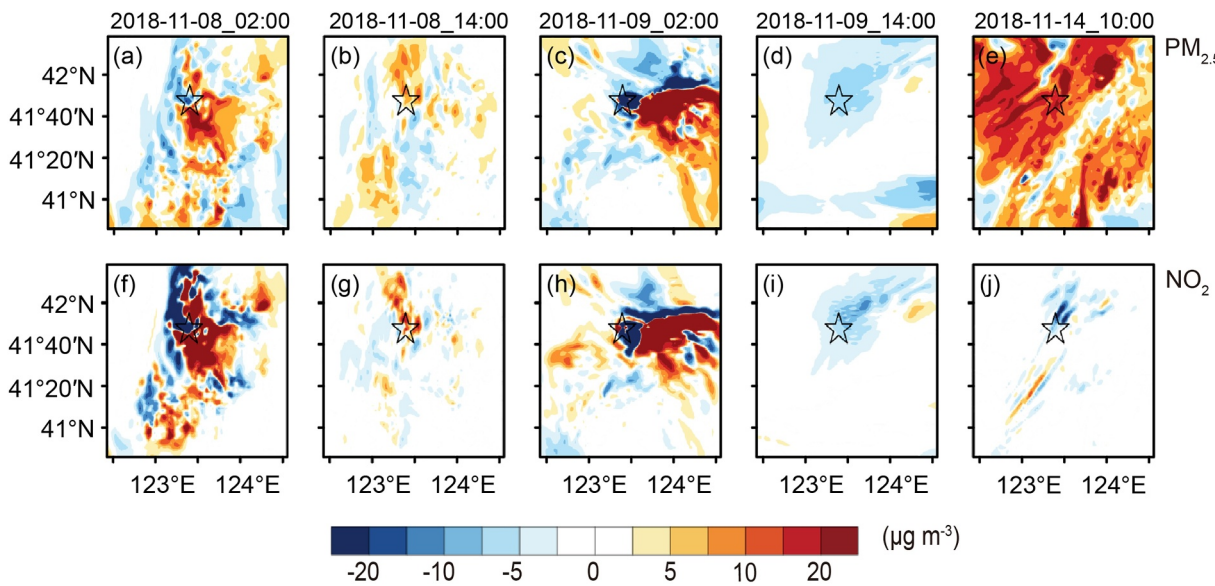


**Figure 10.** The spatial distribution of near-surface concentration differences between the EXP and CTR groups for (a–e) $PM_{2.5}$ and (f–j) $NO_2$ at the selected typical moments. Warm colors indicate higher concentrations in EXP compared to CTR, while cool colors represent the opposite. The stars mark the location of the Shenyang urban area.

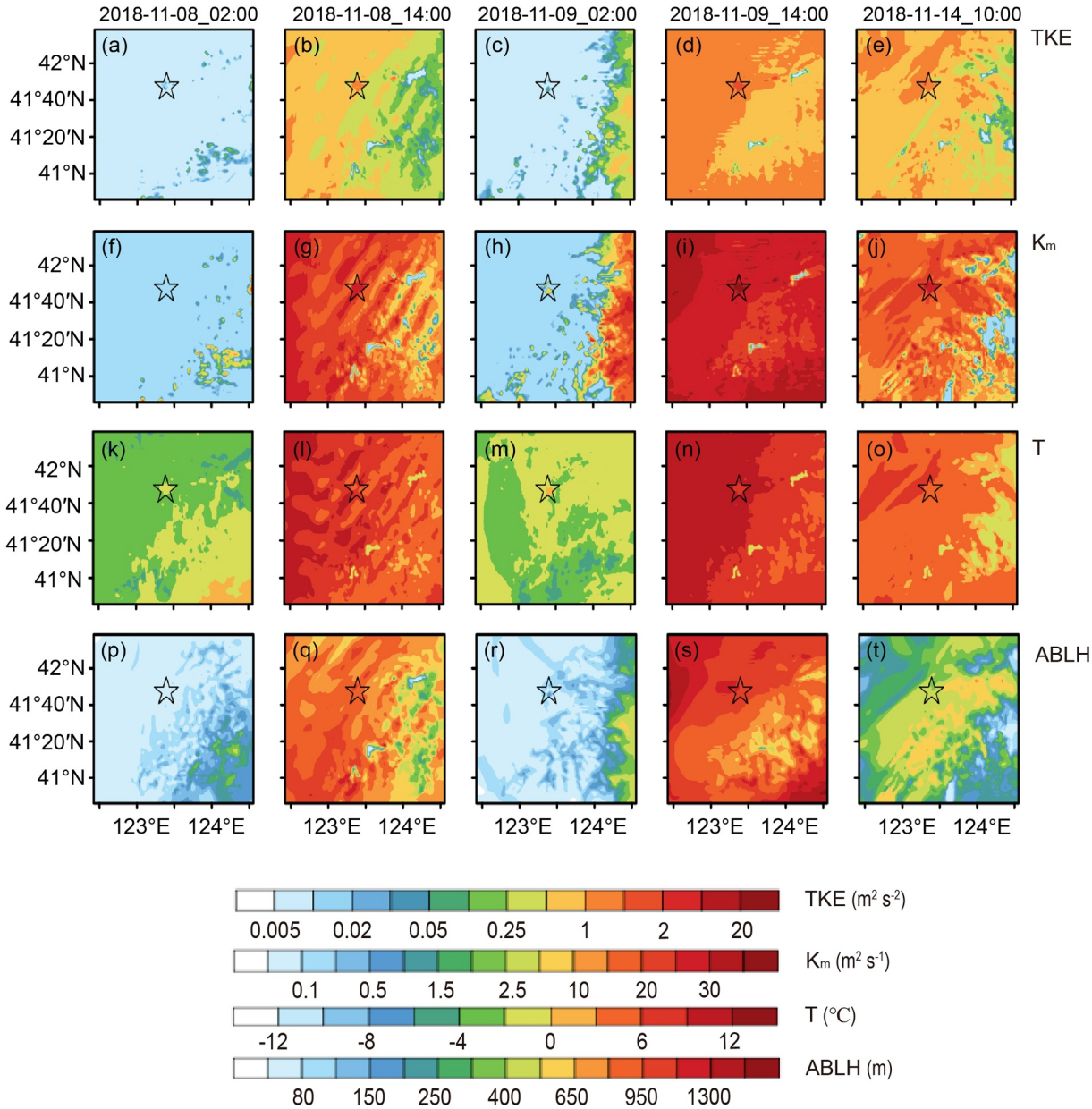


**Figure 11.** The spatial distribution of near-surface (a–e) TKE, (f–j) $K_m$, (k–o) T and (p–t) ABLH in the EXP group at the selected typical moments. Colors indicate their value. The stars mark the location of the Shenyang urban area.

Figures 10a and 10c show that during nighttime, the near-surface $PM_{2.5}$ concentrations in the EXP were lower than those in the CTR over the Shenyang urban area, with a difference of approximately 20 μg $m^{-3}$ around 02:00 LT on November 9. In contrast, the surrounding areas downwind to the southeast exhibited higher $PM_{2.5}$ concentrations in EXP compared to CTR. This phenomenon can be attributed to the slower nocturnal cooling of urban surfaces compared to the surrounding natural land covers. Figure 11 presents the spatial distribution of near-surface (a–e) TKE, (f–j) $K_m$, (k–o) temperature (T), and (p–t) ABLH in the EXP group. As shown in Figures 11a and 11b, near-surface air temperatures over the urban area were significantly higher than those in the surrounding regions during nighttime, particularly at 02:00 LT on November 9, when the temperature between urban area and the surroundings exceeded 6°C. Correspondingly, local TKE and $K_m$ values were also higher within the urban area. As a result, atmospheric turbulence remained more active over urban areas at the same time, enhancing vertical turbulent transport. After applying the HTMC correction, the difference in turbulent diffusion capacity between urban and suburban areas in EXP became even more pronounced. The enhanced turbulence

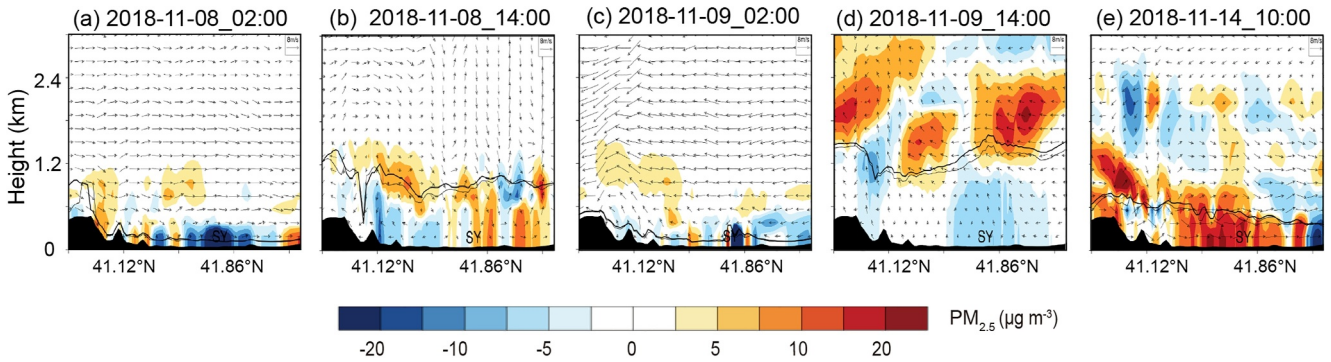


**Figure 12.** The vertical distribution of $PM_{2.5}$ concentration differences between the EXP and CTR groups at the selected typical moments. Warm colors indicate higher concentrations in EXP compared to CTR, while cool colors represent the opposite. The wind speed and direction are the results in EXP. The thinner and thicker black lines represent the ABLH in the CTR and EXP, respectively. The SY shows the location of the Shenyang urban area.

promoted the transport of pollutants from the urban area, where vertical turbulent diffusion was stronger, toward surrounding regions. Consequently, $PM_{2.5}$ concentrations in the suburban areas around the city were higher in EXP than in CTR. The vertical cross-sections of the difference between the two simulation groups shown in Figure 12 indicate that during nighttime, the EXP simulation simulated lower near-surface $PM_{2.5}$ concentrations over Shenyang. Some dispersed to higher altitudes, while others were transported toward downwind suburban areas.

While in the early morning, the urban area warmed more slowly than the surrounding regions, resulting in stronger turbulent vertical diffusion, which promoted the transport and accumulation of pollutants toward the urban area. The EXP exhibited a greater difference in diffusion capacity between urban and suburban areas, enhancing the near-surface transport of $PM_{2.5}$ from surrounding regions into the urban area. Consequently, as shown in Figure 8, $PM_{2.5}$ concentrations in the EXP were higher than those in CTR during the early daytime. In the afternoon, both atmospheric turbulence and the planetary boundary layer were well-developed, significantly enhancing vertical turbulent diffusion compared to nighttime, which led to a rapid decrease in near-surface pollutant concentrations. As discussed in Chapters 3.1–3.2, the original BouLac PBL scheme effectively simulated daytime atmospheric turbulent diffusion. And as shown in Figure 11, the differences in TKE, $K_m$, T, and ABLH between urban and suburban areas during the daytime were relatively small, indicating that the dispersion conditions in the city and surrounding areas were good in both simulation groups during the daytime. Therefore, as shown in Figures 10b and 10d, the concentration differences between the two simulation groups were much smaller during the daytime than at night, with the near-surface $PM_{2.5}$ concentration in the EXP being only about 5 μg $m^{-3}$ lower than that in the CTR. This phenomenon is also evident in Figure 12. In the EXP group, the higher atmospheric boundary layer height and stronger vertical turbulent diffusion facilitated the upward transport of pollutants, resulting in a reduction in near-surface concentrations. However, since daytime dispersion was already relatively sufficient in the CTR group, the concentration differences between the two simulations were significantly smaller than those during nighttime. In contrast, the EP2 exhibited significant differences from EP1. During this episode, there was a significant contribution of pollutant transport from surrounding regions at higher altitudes (shown in Figure 8). The stronger turbulent diffusion in the EXP promoted the downward transport and accumulation of pollutants from the upper. As shown in Figure 10e, the near-surface $PM_{2.5}$ concentrations in the EXP were significantly higher than those in CTR, particularly over the urban area and its surroundings, where this phenomenon was especially pronounced. This is further supported by Figure 12e, which shows that near-surface pollutant concentrations were higher around urban Shenyang in the EXP group, while concentrations aloft were lower. The increased near-surface concentrations are attributed to pollutant transport from surrounding areas.

As one of the key precursors of $PM_{2.5}$, $NO_2$ primarily originates from local emissions, causing its spatiotemporal distribution to be more sensitive to the effects of $K_m$. Figure 13 presents the time series of observed and simulated $NO_2$ concentrations in the Shenyang urban area. The black dots represent observed near-surface $NO_2$ concentrations, while the blue and red dots indicate the simulated values from the CTR and EXP groups, respectively. Shaded areas denote nighttime periods, and the white areas denote daytime periods. Observations show that the $NO_2$ concentrations were generally higher from late afternoon to nighttime compared to the morning, with the

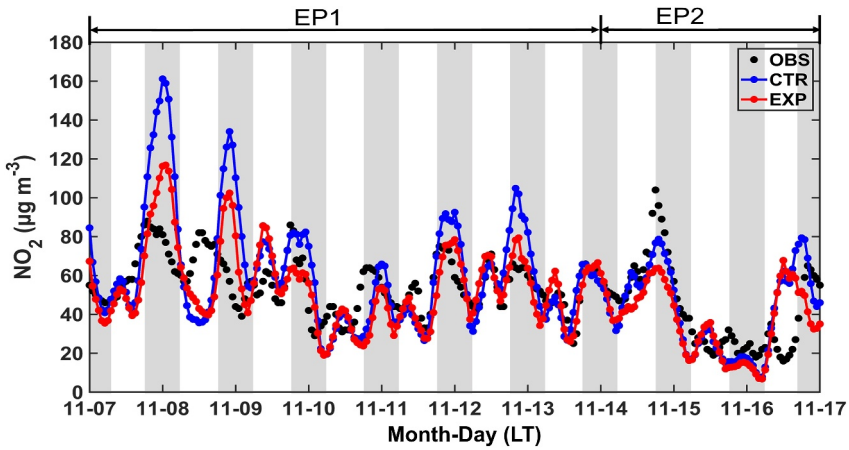


**Figure 13.** Time series of $NO_2$ concentrations over urban Shenyang. The black dots represent observed near-surface concentration, while the red and blue dots indicate simulated concentration in the EXP and CTR groups, respectively. Shaded areas denote nighttime periods, and the white areas denote daytime periods.

highest (approximately 100 μg $m^{-3}$) occurring on the night of November 14. Both simulation groups effectively captured these diurnal variations of $NO_2$ concentrations. However, the EXP showed better agreement with the observed $NO_2$ concentrations in both magnitude and temporal trends. Specifically, during the daytime, the difference between the EXP and CTR was small. While during nighttime, the EXP group simulated significantly lower $NO_2$ concentrations compared to the CTR. Especially in the early morning of November 8, the $NO_2$ concentrations in EXP were lower than those of the CTR by more than 40 μg $m^{-3}$, which were more consistent with the observations.

The scatter plots of simulation and observation of $NO_2$ concentrations (Figure S8 in Supporting Information S1) reveal differences in model performance between the two simulation groups across different periods. During the daytime, observed $NO_2$ concentrations were below 80 μg $m^{-3}$, and the scatter distributions in both the CTR and EXP were largely consistent, with the slopes of the fitted lines differing by only 0.03. This indicates a difference in daytime $NO_2$ simulation performance was small between the two groups. While, at night, observed $NO_2$ concentrations mainly ranged from 50 to 100 μg $m^{-3}$. Most of the scatter points of CTR lay above the $y = x$ reference line, with a fitted slope of 1.42, indicating a significant overestimation of $NO_2$ concentrations. While the fitted slope of EXP was 1.05, showing that its simulated concentration values were much closer to observations. Additionally, statistical indicators in Table 3 further confirm the EXP group had significant improvement in simulating nighttime $NO_2$ concentrations. The bias indicators were reduced by approximately 30% compared to the CTR, and the improvement has passed the significance test.

Figure S7 in Supporting Information S1 shows that during the pollution episode, $NO_2$ exhibited its lowest concentrations around 07:00 and 13:00 LT each day, with a minor peak around 11:00–12:00 LT, and a more pronounced peak occurring between 18:00 and 19:00 LT, reaching values above 60 μg $m^{-3}$. Both the CTR and EXP groups captured this diurnal pattern well. However, the EXP showed a notable improvement in reducing the overestimation of near-surface $NO_2$ concentrations during nighttime, particularly between 22:00 and 03:00 (day + 1) LT.

Figure 14 presents the time series of vertical profiles of $NO_2$ concentrations over the Shenyang urban area for (a) the EXP, (b) the CTR, and (c) the difference in $NO_2$ concentrations between the two simulation groups. In Figures 14a and 14b, the color shading represents $NO_2$ concentrations, while the black solid lines indicate the ABLH. In Figure 14c, the color shading illustrates the concentration differences between the EXP and CTR, with warm colors indicating higher $NO_2$ concentrations in the EXP and cool colors indicating the opposite. The thinner and thicker black solid lines represent the ABLH in the CTR and EXP, respectively. As shown in the figure, there was a sharp decrease in $NO_2$ concentration from the near-surface up to 300 m. The concentration differences between the two simulation groups were larger at night. Specifically, near the surface, $NO_2$ concentrations in the EXP were lower than those in the CTR, while above 100 m, the EXP showed higher concentrations. This phenomenon, consistent with the above analysis, demonstrates that the stronger turbulent diffusion in the EXP enhanced the vertical

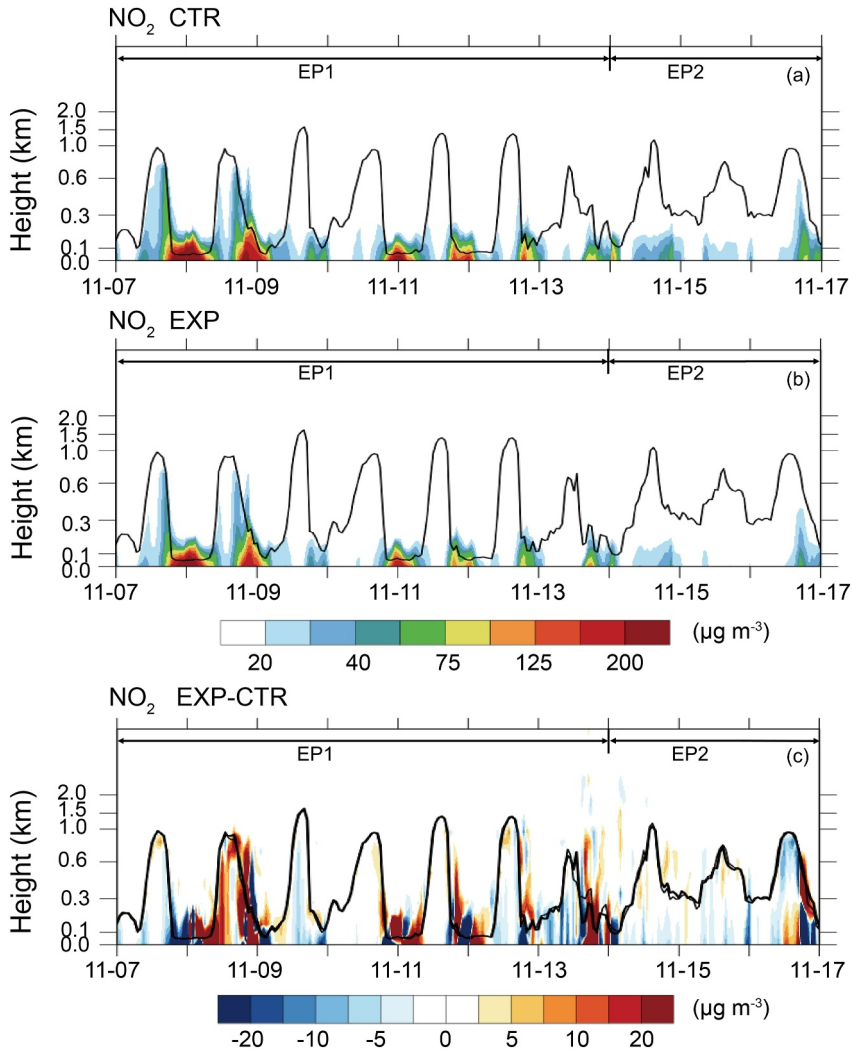


**Figure 14.** Time series of vertical profiles of $NO_2$ concentrations over urban Shenyang in (a) the EXP, (b) the CTR, and (c) the differences between the two simulation groups. The color shading in (a, b) represents $NO_2$ concentrations in each simulation group, and the black solid lines show the simulated ABLH. In (c), warm colors indicate higher $NO_2$ concentrations in EXP and cool colors indicate the opposite. The thinner and thicker black lines represent the ABLH in the CTR and EXP, respectively.

transport of $NO_2$ at night. The upward transport in the EXP led to concentration differences exceeding 20 μg $m^{-3}$ compared to the CTR. During the daytime, vertical concentration differences between the two groups also existed but were generally less than 5 μg $m^{-3}$. These findings confirm the critical role of high-frequency TKE in pollutant dispersion under stable nighttime conditions. Meanwhile, the $NO_2$ concentration differences between the EXP and CTR, driven by high-frequency turbulence, were more pronounced than those for $PM_{2.5}$.

Figures 10f–10j show the spatial distribution of near-surface $NO_2$ concentration differences between the EXP and CTR at typical moments. During the EP1, the $NO_2$ concentration differences were consistent with those of $PM_{2.5}$, showing lower concentrations over urban Shenyang and higher concentrations in the surrounding areas in the EXP compared to the CTR. This concentration difference was more significant at night than during the daytime. However, during the EP2, near-surface $NO_2$ concentrations in the EXP were lower than those in the CTR over urban areas, which was opposite to the $PM_{2.5}$ concentration difference. As a pollutant primarily derived from local emissions, there was no vertical transport of $NO_2$ from higher altitudes. Consequently, the concentration differences between the two simulation groups mostly exhibited the following pattern: lower $NO_2$ concentrations in the EXP group within urban areas and higher concentrations in the surrounding regions. Furthermore, as a

pollutant influenced mainly by local emissions, $NO_2$ was more sensitive to differences in atmospheric turbulent diffusion. Therefore, after applying the HTMC correction, the $NO_2$ concentration differences between the EXP and CTR were greater than those of $PM_{2.5}$. This further demonstrates that high-frequency turbulent kinetic energy has a more significant influence on the spatiotemporal distribution of pollutants from local emissions.

## 4. Conclusions

This study was based on high-frequency and low-frequency wind speed observations obtained from ultrasonic anemometers and cup anemometers at various heights on the 325-m meteorological tower in Beijing. Based on the −5/3 law of the turbulence energy spectrum theory, we first conducted an in-depth analysis of how the cutoff frequency of wind speed time series contributes to the underestimation of atmospheric turbulent kinetic energy (TKE). To address this issue, we proposed a High-frequency TKE Modification Coefficient (HTMC) scheme and parameterized it into the BouLac planetary boundary layer scheme of WRF-Chem. Numerical sensitivity experiments and observational validation were performed for a heavy haze pollution event in the Shenyang urban agglomeration in November 2018. The main points are as follows:

1. When the temporal resolution of wind speed time series (such as the sampling frequency of observations or the integration time step in models) is lower than the atmospheric turbulence dissipation frequency, the miss of high-frequency or small-scale turbulent eddies leads to a systematic underestimation of TKE. This underestimation becomes more significant as the sampling frequency decreases.
2. The observation analysis shows that when the sampling frequency is about 0.05 Hz, the underestimation range of TKE is 10%–37%, the missing at night is greater than that at daytime, and the missing in winter is greater than that in summer. The maximum underestimation of about 37% occurs at night in winter, while the minimum underestimation of about 10% occurs during daytime in summer. Therefore, it is necessary to introduce HTMC into the turbulence model.
3. The HTMC factor is incorporated into the BouLac PBL scheme of WRF-Chem for numerical sensitivity experiments and observational validation. The modified Improved BouLac scheme enhances the vertical turbulence diffusion capacity near the surface, promoting the vertical diffusion of $PM_{2.5}$ and $NO_2$, which results in simulated concentrations that are more consistent with the observations. The correction is particularly effective at night, where the impact on pollutant diffusion is more significant. The simulation bias for $PM_{2.5}$ at night decreases from 23.77% in the control group to 6.18% in the EXP, and for $NO_2$, the bias decreases from 16.30% to 5.67%. This correction significantly reduces the underestimation of atmospheric turbulence energy, especially under special meteorological conditions such as low wind speeds and temperature inversions, thereby improving the accuracy of TKE and diffusion coefficient simulations.

In summary, in this study the HTMC scheme was developed to improve the TKE simulation by considering the contribution of high-frequency turbulence kinetic energy. Then by introducing the HTMC scheme into the WRF-Chem, the performance of the WRF-Chem model in simulating urban haze pollution events was successfully improved. This provides valuable insights for future improvements in atmospheric pollution prediction models. Future research could further explore the applicability and scalability of this correction scheme under different geographical environments and meteorological conditions.

## Conflict of Interest

The authors declare no conflicts of interest relevant to this study.

## Data Availability Statement

The input data for simulation by WRF-Chem, the code for the HTMC scheme proposed in this study, the BouLac boundary layer scripts that call this HTMC subroutine (including both the official and modified versions), and the observation and simulation data of near-surface meteorological environmental elements in urban Shenyang are all available at Liu et al. (2025).

**Acknowledgments**
This work was supported by the National Key Research and Development Program of China (2024YFC3013004), the National Natural Science Foundation of China (U234221) and the Open fund by Jiangsu Key Laboratory of Atmospheric Environment Monitoring and Pollution Control (BK20220031). We acknowledge the High-Performance Computing Centre of Nanjing University of Information Science and Technology for their support of this work.

## References

Acosta, T., Guo, Y., Wang, J., Brusco, S., & Kopp, G. A. (2024). Requirements for partial turbulence simulations using nondimensional turbulence energy contributions. *Journal of Wind Engineering and Industrial Aerodynamics*, *254*, 105886. https://doi.org/10.1016/j.jweia.2024.105886

Aliabadi, A., Moradi, M., & Byerlay, R. (2021). The budgets of turbulence kinetic energy and heat in the urban roughness sublayer. *Environmental Fluid Mechanics*, *21*(4), 843–884. https://doi.org/10.1007/s10652-021-09800-x

Banks, R., Tiana-Alsina, J., Baldasano, J., Rocadenbosch, F., Papayannis, A., Solomos, S., & Tzanis, C. G. (2016). Sensitivity of boundary-layer variables to PBL schemes in the WRF model based on surface meteorological observations, lidar, and radiosondes during the HygrA-CD campaign. *Atmospheric Research*, *176–177*, 185–201. https://doi.org/10.1016/j.atmosres.2016.02.024

Barlow, J. (2014). Progress in observing and modelling the urban boundary layer. *Urban Climate*, *10*, 216–240. https://doi.org/10.1016/j.uclim.2014.03.011

Bodini, N., Lundquist, J., Krishnamurthy, R., Pekour, M., Berg, L. K., & Choukulkar, A. (2019). Spatial and temporal variability of turbulence dissipation rate in complex terrain. *Atmospheric Chemistry and Physics*, *19*(7), 4367–4382. https://doi.org/10.5194/acp-19-4367-2019

Bougeault, P., & Lacarrere, P. (1989). Parameterization of orography-induced turbulence in a Mesobeta--Scale model. *Monthly Weather Review*, *117*(8), 1872–1890. https://doi.org/10.1175/1520-0493(1989)117<1872:POOITI>2.0.CO;2

Chen, Y., An, J., Sun, Y., Wang, X., Qu, Y., Zhang, J., et al. (2018). Nocturnal low-level winds and their impacts on particulate matter over the Beijing Area. *Advances in Atmospheric Sciences*, *35*(12), 1455–1468. https://doi.org/10.1007/s00376-018-8022-9

Chiravalle, V. (2006). The k-L turbulence model for describing buoyancy-driven fluid instabilities. *Laser and Particle Beams*, *24*(3), 381–394. https://doi.org/10.1017/S026303460606054X

Dong, S., Huang, Y., Yuan, X., & Lozano-Durán, A. (2020). The coherent structure of the kinetic energy transfer in shear turbulence. *Journal of Fluid Mechanics*, *892*, A22. https://doi.org/10.1017/jfm.2020.195

Du, Q., Zhao, C., Zhang, M., Dong, X., Chen, Y., Liu, Z., et al. (2020). Modeling diurnal variation of surface $PM_{2.5}$ concentrations over East China with WRF-Chem: Impacts from boundary-layer mixing and anthropogenic emission. *Atmospheric Chemistry and Physics*, *20*(5), 2839–2863. https://doi.org/10.5194/acp-20-2839-2020

Guo, J., Miao, Y., Zhang, Y., Liu, H., Li, Z., Zhang, W., et al. (2016). The climatology of planetary boundary layer height in China derived from radiosonde and reanalysis data. *Atmospheric Chemistry and Physics*, *16*(20), 13309–13319. https://doi.org/10.5194/acp-16-13309-2016

Heinl, M., Hammerle, A., Tappeiner, U., & Leitinger, G. (2015). Determinants of urban–rural land surface temperature differences—A landscape scale perspective. *Landscape and Urban Planning*, *134*, 33–42. https://doi.org/10.1016/j.landurbplan.2014.10.003

Holtslag, A., & Boville, B. (1993). Local versus nonlocal boundary-layer diffusion in a global climate model. *Journal of Climate*, *6*(10), 1825–1842. https://doi.org/10.1175/1520-0442(1993)006<1825:LVNBLD>2.0.CO;2

Honnert, R. (2019). Grey-zone turbulence in the neutral atmospheric boundary layer. *Boundary-Layer Meteorology*, *170*(2), 191–204. https://doi.org/10.1007/s10546-018-0394-y

Honnert, R., Masson, V., Lac, C., & Nagel, T. (2021). A theoretical analysis of mixing length for atmospheric models from micro to large scales. *Frontiers in Earth Science*, *8*, 582056. https://doi.org/10.3389/feart.2020.582056

Huang, Y., & Peng, X. (2017). Improvement of the Mellor–Yamada–Nakanishi–Niino planetary boundary-layer scheme based on observational data in China. *Boundary-Layer Meteorology*, *162*(1), 171–188. https://doi.org/10.1007/s10546-016-0187-0

Huo, Y., Wang, Y., Paasonen, P., Liu, Q., Tang, G., Ma, Y., et al. (2021). Trends of planetary boundary layer height over urban cities of China from 1980–2018. *Frontiers in Environmental Science*, *9*, 744255. Original Research. https://doi.org/10.3389/fenvs.2021.744255

Huszar, P., Karlicky, J., Doubalová, J., Šindelářová, K., Nováková, T., Belda, M., et al. (2020). Urban canopy meteorological forcing and its impact on ozone and $PM_{2.5}$: Role of vertical turbulent transport. *Atmospheric Chemistry and Physics*, *20*(4), 1977–2016. https://doi.org/10.5194/acp-20-1977-2020

Jia, W., & Zhang, X. (2021). Impact of modified turbulent diffusion of PM2.5 aerosol in WRF-Chem simulations in eastern China. *Atmospheric Chemistry and Physics*, *21*(22), 16827–16841. https://doi.org/10.5194/acp-21-16827-2021

Jia, W., Zhang, X., Zhang, H., & Ren, Y. (2021). Application of turbulent diffusion term of aerosols in mesoscale model. *Geophysical Research Letters*, *48*(11), e2021GL093199. https://doi.org/10.1029/2021GL093199

Josserand, C., LeBerre, M., Lehner, T., & Pomeau, Y. (2017). Turbulence: Does energy cascade exist? *Journal of Statistical Physics*, *167*(3), 596–625. https://doi.org/10.1007/s10955-016-1642-5

Junninen, H., Niska, H., Tuppurainen, K., Ruuskanen, J., & Kolehmainen, M. (2004). Methods for imputation of missing values in air quality data sets. *Atmospheric Environment*, *38*(18), 2895–2907. https://doi.org/10.1016/j.atmosenv.2004.02.026

Kim, E., Choi, K., Park, S., Kim, M. H., Kim, S. W., Park, M. S., et al. (2023). Turbulent characteristics in complex coastal areas assessed using BSWO observations and WRF-LES simulation results. *Atmospheric Research*, *289*, 106756. https://doi.org/10.1016/j.atmosres.2023.106756

Kit, E., Hocut, C. M., Liberzon, D., & Fernando, H. J. S. (2017). Fine-scale turbulent bursts in stable atmospheric boundary layer in complex terrain. *Journal of Fluid Mechanics*, *833*, 745–772. https://doi.org/10.1017/jfm.2017.717

Krayenhoff, E., Santiago, J., Martilli, A., Christen, A., & Oke, T. R. (2015). Parametrization of drag and turbulence for urban neighbourhoods with trees. *Boundary-Layer Meteorology*, *156*(2), 157–189. https://doi.org/10.1007/s10546-015-0028-6

Li, B., Shi, X., Liu, Y., Lu, L., Wang, G. l., Thapa, S., et al. (2020). Long-term characteristics of criteria air pollutants in megacities of Harbin-Changchun megalopolis, Northeast China: Spatiotemporal variations, source analysis, and meteorological effects. *Environmental Pollution*, *267*, 115441. https://doi.org/10.1016/j.envpol.2020.115441

Li, C., Liu, M., Hu, Y., Zhou, R., Huang, N., & Wu, W. (2020). Spatial distribution characteristics of gaseous pollutants and particulate matter inside a city in the heating season of Northeast China. *Sustainable Cities and Society*, *61*, 102302. https://doi.org/10.1016/j.scs.2020.102302

Li, J., Gao, W., Cao, L., He, L., Zhang, X., Yan, Y., et al. (2021). Effects of different stagnant meteorological conditions on aerosol chemistry and regional transport changes in Beijing, China. *Atmospheric Environment*, *258*, 118483. https://doi.org/10.1016/j.atmosenv.2021.118483

Li, J., Sun, L., Yao, X., Zang, S., Wang, J., & Ma, D. (2023). Attributions of emission-reduction and meteorological conditions to typical heavy pollution episodes in a cold metropolis, northeast China. *Frontiers in Environmental Science*, *11*, 1331536. https://doi.org/10.3389/fenvs.2023.1331536

Li, Q., & Katul, G. (2022). Bridging the urban canopy sublayer to aerodynamic parameters of the atmospheric surface layer. *Boundary-Layer Meteorology*, *185*(1), 35–61. https://doi.org/10.1007/s10546-022-00723-8

Li, Q., Wu, B., Liu, J., Zhang, H., Cai, X., & Song, Y. (2020). Characteristics of the atmospheric boundary layer and its relation with $PM_{2.5}$ during haze episodes in winter in the North China Plain. *Atmospheric Environment*, *223*, 117265. https://doi.org/10.1016/j.atmosenv.2020.117265

Li, X., Ma, Y., Wang, Y., Liu, N., & Hong, Y. (2017). Temporal and spatial analyses of particulate matter (PM10 and $PM_{2.5}$) and its relationship with meteorological parameters over an urban city in northeast China. *Atmospheric Research*, *198*, 185–193. https://doi.org/10.1016/j.atmosres.2017.08.023

Li, X., Ma, Y., Wei, W., Zhang, Y., Liu, N., & Hong, Y. (2019). Vertical distribution of particulate matter and its relationship with planetary boundary layer structure in Shenyang, Northeast China. *Aerosol and Air Quality Research*, *19*(11), 2464–2476. https://doi.org/10.4209/aaqr.2019.06.0311

Liu, D., Yan, W., Kang, Z., Liu, A., & Zhu, Y. (2018). Boundary-layer features and regional transport process of an extreme haze pollution event in Nanjing, China. *Atmospheric Pollution Research*, *9*(6), 1088–1099. https://doi.org/10.1016/j.apr.2018.04.009

Liu, L., Shi, Y., Zhang, Z., Zhang, K., & Hu, F. (2023). Analysis of turbulence intensity in the megacity of Beijing by high-frequency observations on a 325-m Tower. *Renewable Energy*, *217*, 119184. https://doi.org/10.1016/j.renene.2023.119184

Liu, Y., Li, Q., Yang, L., Mu, K., Zhang, M., & Liu, J. (2020). Urban heat island effects of various urban morphologies under regional climate conditions. *Science of the Total Environment*, *743*, 140589. https://doi.org/10.1016/j.scitotenv.2020.140589

Liu, Y., Liu, C., Brasseur, G., & Chao, C. Y. (2023). Wavelet analysis of the atmospheric flows over real urban morphology. *Science of the Total Environment*, *859*, 160209. https://doi.org/10.1016/j.scitotenv.2022.160209

Liu, Z., Chen, Y., Wang, Y., Liu, C., Liu, S., & Liao, H. (2023). The development and validation of the Inhomogeneous Wind Scheme for Urban Street (IWSUS-v1). *Geoscientific Model Development*, *16*(15), 4385–4403. https://doi.org/10.5194/gmd-16-4385-2023

Liu, Z., Zhang, W., Liu, L., Li, X., Mao, Y., & Liao, H. (2025). Quantifying high-frequency turbulence energy in the atmosphere and its impact on near-surface diffusion: Parameterization scheme and validation in WRF-Chem [Dataset]. *Zenodo*. https://doi.org/10.5281/zenodo.16885432

Lv, Y., Guo, J., Li, J., Cao, L., Chen, T., Wang, D., et al. (2021). Spatiotemporal characteristics of atmospheric turbulence over China estimated using operational high-resolution soundings. *Environmental Research Letters*, *16*(5), 054050. https://doi.org/10.1088/1748-9326/abf461

Ma, Y., Wang, Y., Xian, T., Tian, G., Lu, C., Mao, X., & Wang, L. P. (2024). Impact of PBL schemes on multiscale WRF modeling over complex terrain, Part I: Mesoscale simulations. *Atmospheric Research*, *297*, 107117. https://doi.org/10.1016/j.atmosres.2023.107117

Martilli, A., Clappier, A., & Rotach, M. (2002). An urban surface exchange parameterisation for mesoscale models. *Boundary-Layer Meteorology*, *104*(2), 261–304. https://doi.org/10.1023/A:1016099921195

McCaffrey, K., Bianco, L., & Wilczak, J. (2017). Improved observations of turbulence dissipation rates from wind profiling radars. *Atmospheric Measurement Techniques*, *10*(7), 2595–2611. https://doi.org/10.5194/amt-10-2595-2017

Monnier, B., Goudarzi, S., Vinuesa, R., & Wark, C. (2018). Turbulent structure of a simplified urban fluid flow studied through stereoscopic particle image velocimetry. *Boundary-Layer Meteorology*, *166*(2), 239–268. https://doi.org/10.1007/s10546-017-0303-9

Nakanishi, M., & Niino, H. (2009). Development of an improved turbulence closure model for the atmospheric boundary layer. *Journal of the Meteorological Society of Japan. Ser. II*, *87*(5), 895–912. https://doi.org/10.2151/jmsj.87.895

Obukhov, A. (1971). Turbulence in an atmosphere with a non-uniform temperature. *Boundary-Layer Meteorology*, *2*(1), 7–29. https://doi.org/10.1007/BF00718085

Pielke, R., & Mahrer, Y. (1975). Representation of the heated planetary boundary layer in mesoscale models with coarse vertical resolution. *Journal of the Atmospheric Sciences*, *32*(12), 2288–2308. https://doi.org/10.1175/1520-0469(1975)032<2288:ROTHPB>2.0.CO;2

Ren, Y., Zhang, H., Wei, W., Wu, B., Cai, X., & Song, Y. (2019). Effects of turbulence structure and urbanization on the heavy haze pollution process. *Atmospheric Chemistry and Physics*, *19*(2), 1041–1057. https://doi.org/10.5194/acp-19-1041-2019

Ren, Y., Zhang, H., Wei, W., Wu, B., Liu, J., Cai, X., & Song, Y. (2019). Comparison of the turbulence structure during light and heavy haze pollution episodes. *Atmospheric Research*, *230*, 104645. https://doi.org/10.1016/j.atmosres.2019.104645

Ruan, Z., Mu, R., Wei, M., & Ge, R. (2014). Spectrum analysis of wind profiling radar measurements. *Journal of Meteorological Research*, *28*(4), 656–667. https://doi.org/10.1007/s13351-014-3171-y

Shao, X., Zhang, N., Li, D., & Sun, J. (2024). On the size of dominant momentum transporting eddies in stable atmospheric boundary layers. *Geophysical Research Letters*, *51*(23), e2024GL111459. https://doi.org/10.1029/2024GL111459

Shi, L., Zhu, A., Huang, L., Yaluk, E., Gu, Y., Wang, Y., et al. (2021). Impact of the planetary boundary layer on air quality simulations over the Yangtze River Delta region, China. *Atmospheric Environment*, *263*, 118685. https://doi.org/10.1016/j.atmosenv.2021.118685

Shi, Y., Hu, F., Lü, R., & He, Y. (2019). Characteristics of urban boundary layer in heavy haze process based on Beijing 325m tower data. *Atmospheric and Oceanic Science Letters*, *12*(1), 41–49. https://doi.org/10.1080/16742834.2019.1547084

Theuerkauf, A., Gerding, M., & Lübken, F. (2011). LITOS—A new balloon-borne instrument for fine-scale turbulence soundings in the stratosphere. *Atmospheric Measurement Techniques*, *4*(1), 55–66. https://doi.org/10.5194/amt-4-55-2011

Vassilicos, J. (2015). Dissipation in turbulent flows. *Annual Review of Fluid Mechanics*, *47*(1), 95–114. https://doi.org/10.1146/annurev-fluid-010814-014637

Vogelezang, D., & Holtslag, A. (1996). Evaluation and model impacts of alternative boundary-layer height formulations. *Boundary-Layer Meteorology*, *81*(3), 245–269. https://doi.org/10.1007/BF02430331

Wang, A., Li, Y., Zhao, C., Du, Q., Wang, X., & Gao, Z. (2021). Influence of different boundary layer schemes on $PM_{2.5}$ concentration simulation in Nanjing. *China Environmental Science*, *41*(7), 2977–2992. https://doi.org/10.19674/i.cnki.issn1000-6923.2021.0301

Wei, W., Zhang, H., Wu, B., Huang, Y., Cai, X., Song, Y., & Li, J. (2018). Intermittent turbulence contributes to vertical dispersion of $PM_{2.5}$ in the North China Plain: Cases from Tianjin. *Atmospheric Chemistry and Physics*, *18*(17), 12953–12967. https://doi.org/10.5194/acp-18-12953-2018

Wu, S., Chen, C., Song, H., Yu, Z., Wang, J., & Wang, Y. (2024). Reduced-scale numerical simulation method and its application to urban-scale buoyancy-driven flows. *Building and Environment*, *249*, 111117. https://doi.org/10.1016/j.buildenv.2023.111117

Xian, J., Lu, C., Lin, X., Yang, H., Zhang, N., & Zhang, L. (2024). Directly measuring the power-law exponent and kinetic energy of atmospheric turbulence using coherent Doppler wind lidar. *Atmospheric Measurement Techniques*, *17*(6), 1837–1850. https://doi.org/10.5194/amt-17-1837-2024

Xian, J., Luo, H., Lu, C., Lin, X., Yang, H., & Zhang, N. (2024). Characteristics of the atmospheric boundary layer height: A perspective on turbulent motion. *Science of the Total Environment*, *919*, 170895. https://doi.org/10.1016/j.scitotenv.2024.170895

Xu, D., Wang, Y., Zhou, D., Zhang, Q., & Yang, Y. (2024). Influences of urban spatial factors on surface urban heat island effect and its spatial heterogeneity: A case study of Xi'an. *Building and Environment*, *248*, 111072. https://doi.org/10.1016/j.buildenv.2023.111072

Xu, H., Wang, H., & Duan, Y. (2021). An investigation of the impact of different turbulence schemes on the tropical cyclone boundary layer at turbulent gray-zone resolution. *Journal of Geophysical Research: Atmospheres*, *126*(21), e2021JD035327. https://doi.org/10.1029/2021JD035327

Yao, L., Liu, C., Brasseur, G., & Chao, C. Y. (2024). Turbulent flow modification in the atmospheric surface layer over a dense city. *Science of the Total Environment*, *909*, 168315. https://doi.org/10.1016/j.scitotenv.2023.168315

Zhang, J., Liu, L., Xu, L., Lin, Q., Zhao, H., Wang, Z., et al. (2020). Exploring wintertime regional haze in northeast China: Role of coal and biomass burning. *Atmospheric Chemistry and Physics*, *20*(9), 5355–5372. https://doi.org/10.5194/acp-20-5355-2020

Zhang, W., Fung, J., & Wong, M. (2024). An improved non-local planetary boundary layer parameterization scheme in weather forecasting and research model based on a 1.5-order turbulence closure model. *Journal of Geophysical Research: Atmospheres*, *129*(12), e2023JD040432. https://doi.org/10.1029/2023JD040432

Zhao, D., Liu, G., Xin, J., Quan, J., Wang, Y., Wang, X., et al. (2020). Haze pollution under a high atmospheric oxidization capacity in summer in Beijing: Insights into formation mechanism of atmospheric physicochemical processes. *Atmospheric Chemistry and Physics*, *20*(8), 4575–4592. https://doi.org/10.5194/acp-20-4575-2020

Zhong, Q., Ma, J., Shen, G., Shen, H., Zhu, X., Yun, X., et al. (2018). Distinguishing emission-associated ambient Air $PM_{2.5}$ concentrations and meteorological factor-induced fluctuations. *Environmental Science & Technology*, *52*(18), 10416–10425. https://doi.org/10.1021/acs.est.8b02685

Zilitinkevich, S., Elperin, T., Kleeorin, N., Rogachevskii, I., & Esau, I. (2013). A hierarchy of Energy- and Flux-Budget (EFB) turbulence closure models for stably-stratified geophysical flows. *Boundary-Layer Meteorology*, *146*(3), 341–373. https://doi.org/10.1007/s10546-012-9768-8